

# Signatures of Electrical Stimulation Driven Network Interactions in the Human Limbic System

Gabriela Ojeda Valencia,<sup>1</sup> Nicholas M. Gregg,<sup>2</sup> Harvey Huang,<sup>3</sup> Brian N. Lundstrom,<sup>2</sup> Benjamin H. Brinkmann,<sup>2</sup> Tal Pal Attia,<sup>1</sup> Jamie J. Van Gompel,<sup>4</sup> Matt A. Bernstein,<sup>5</sup> Myung-Ho In,<sup>5</sup> John Huston III,<sup>5</sup> Gregory A. Worrell,<sup>1,2</sup> Kai J. Miller,<sup>1,4</sup> and Dora Hermes<sup>1</sup>

<sup>1</sup>Department of Physiology and Biomedical Engineering, Mayo Clinic Rochester, Rochester, Minnesota 55902, <sup>2</sup>Department of Neurology, Mayo Clinic Rochester, Rochester, Minnesota 55902, <sup>3</sup>Mayo Clinic Medical Scientist Training Program, Mayo Clinic Rochester, Rochester, Minnesota 55902, <sup>4</sup>Department of Neurologic Surgery, Mayo Clinic Rochester, Rochester, Minnesota 55902, and <sup>5</sup>Department of Radiology, Mayo Clinic Rochester, Rochester, Minnesota 55902

Stimulation-evoked signals are starting to be used as biomarkers to indicate the state and health of brain networks. The human limbic network, often targeted for brain stimulation therapy, is involved in emotion and memory processing. Previous anatomic, neurophysiological, and functional studies suggest distinct subsystems within the limbic network (Rolls, 2015). Studies using intracranial electrical stimulation, however, have emphasized the similarities of the evoked waveforms across the limbic network. We test whether these subsystems have distinct stimulation-driven signatures. In eight patients (four male, four female) with drug-resistant epilepsy, we stimulated the limbic system with single-pulse electrical stimulation. Reliable corticocortical evoked potentials (CCEPs) were measured between hippocampus and the posterior cingulate cortex (PCC) and between the amygdala and the anterior cingulate cortex (ACC). However, the CCEP waveform in the PCC after hippocampal stimulation showed a unique and reliable morphology, which we term the “limbic Hippocampus-Anterior nucleus of the thalamus-Posterior cingulate, HAP-wave.” This limbic HAP-wave was visually distinct and separately decoded from the CCEP waveform in ACC after amygdala stimulation. Diffusion MRI data show that the measured end points in the PCC overlap with the end points of the parolfactory cingulum bundle rather than the parahippocampal cingulum, suggesting that the limbic HAP-wave may travel through fornix, mammillary bodies, and the anterior nucleus of the thalamus (ANT). This was further confirmed by stimulating the ANT, which evoked the same limbic HAP-wave but with an earlier latency. Limbic subsystems have unique stimulation-evoked signatures that may be used in the future to help network pathology diagnosis.

**Key words:** connectivity; electrophysiology; iEEG; limbic system; networks; posterior cingulate cortex

## Significance Statement

The limbic system is often compromised in diverse clinical conditions, such as epilepsy or Alzheimer’s disease, and characterizing its typical circuit responses may provide diagnostic insight. Stimulation-evoked waveforms have been used in the motor system to diagnose circuit pathology. We translate this framework to limbic subsystems using human intracranial stereo EEG (sEEG) recordings that measure deeper brain areas. Our sEEG recordings describe a stimulation-evoked waveform characteristic to the memory and spatial subsystem of the limbic network that we term the “limbic HAP-wave.” The limbic HAP-wave follows anatomic white matter pathways from hippocampus to thalamus to the posterior cingulum and shows promise as a distinct biomarker of signaling in the human brain memory and spatial limbic network.

Received Nov. 29, 2022; revised Aug. 4, 2023; accepted Aug. 8, 2023.

Author contributions: G.O.V., N.M.G., B.N.L., G.A.W., K.J.M., and D.H. designed research; G.O.V., N.M.G., H.H., B.N.L., J.J.V.G., M.A.B., M.-H.I., J.H., G.A.W., K.J.M., and D.H. performed research; H.H., M.A.B., M.-H.I., K.J.M., and D.H. contributed unpublished reagents/analytic tools; G.O.V., H.H., B.H.B., T.P.A., and D.H. analyzed data; G.O.V. and D.H. wrote the paper.

This research was supported by the Mayo Clinic DERIVE Office and the Mayo Clinic Center for Biomedical Discovery support, and by the National Institute of Mental Health of the National Institutes of Health under Grant R01-MH-122258. The content is solely the responsibility of the authors and does not necessarily represent the official views of the National Institutes of Health. We thank all subjects enrolled in the study, and Cindy Nelson and Karla Crockett for the assistance provided.

N.M.G. is a coinvestigator for the Medtronic EPAS trial, and an industry consultant (NeuroOne, funds to Mayo Clinic). G.A.W. declares intellectual property disclosures related to behavioral state, seizure detection, and seizure forecasting algorithms. Intellectual property has been licensed to Cadence Neuroscience and NeuroOne. B.N.L. declares intellectual

property licensed to Cadence Neuroscience (contractual rights waived) and Seer Medical (contractual rights waived); and has been a site investigator (Medtronic EPAS, NeuroPace RESPONSE, Neuroelectrics tDCS for Epilepsy) and industry consultant (Epiminder, Medtronic, Neuropace, Philips Neuro; funds to Mayo Clinic). J.J.V.G. was named inventor for intellectual property licensed to Cadence Neuroscience Inc, which is co-owned by Mayo Clinic, and has been an investigator for the Medtronic EPAS trial, the SLATE trial, and Mayo Clinic Medtronic NIH Public Private Partnership (UH3-NS95495); has owned stock in and has had a consulting contract with Neuro-One; and has been site Primary Investigator in the Polyganics ENCASE II trial, site Primary Investigator in the NXDC Gleolan Men301 trial, and site Primary Investigator in the Insightec MRgUS EP001 trial; M.A.B. is a former employee of GE Medical Systems and receives pension payments. The authors declare no other competing financial interests.

Correspondence should be addressed to Dora Hermes at [Hermes.Dora@mayo.edu](mailto:Hermes.Dora@mayo.edu).

<https://doi.org/10.1523/JNEUROSCI.2201-22.2023>

Copyright © 2023 the authors

## Introduction

Describing stimulation-evoked biomarkers of specific human brain circuits has greatly advanced the understanding of different brain functions. Studies in the motor system, for instance, described D-waves and I-waves as evoked by direct and indirect excitation (Patton and Amassian, 1954; Awiszus and Feistner, 1994). In other cortical circuits, however, the focus has often been on extracting similar waveforms across connections. Single-pulse electrical stimulation (SPES) often evokes negative electrical potential responses in directly connected regions within 50 ms [first negative component (N1)], which has been related to direct corticocortical projections (Keller et al., 2014). Recent work has highlighted how the focus on early responses has left out components with different timescales and morphologies (Gronlier et al., 2021; Miller et al., 2023), crucial to unriddling complex cortico-subcortical pathways. Given the important role of the limbic system in neurologic diseases, understanding its stimulation-driven features can help advance technologies that target this system.

In 1878, Paul Broca used the term “limbic” (Latin for “border”) for the first time to name the brain structures located on the border between cortical and subcortical regions, composed of the cingulate, hippocampal gyri, and the subcallosal frontal area (Bubb et al., 2017). In 1937, connectivity among the hippocampal complex (HC), mammillary body (MB), anterior nucleus of the thalamus (ANT), and the cingulate cortex was proposed by James Papez as a functional model for emotions (Papez, 1937). Later, in 1949, Paul MacLean built on the previous work of Papez (1937) and coined the widely used term “limbic system,” with other cognitive associations (MacLean, 1949 and Squire, 1998). More recent studies have shown that there are multiple subdivisions in the limbic system based on cytoarchitecture with distinct functional roles [amygdala (Amg) and anterior cingulate cortex (ACC) vs hippocampus and posterior cingulate cortex (PCC); Rolls, 2015; Vogt, 2019].

The limbic system also plays a critical role in clinical conditions, such as epilepsy (Bertram et al., 1998; Salanova et al., 2015; Jo et al., 2019), Alzheimer’s disease (Luo et al., 2021), depression (Holtzheimer et al., 2012; Siddiqi et al., 2021), and obsessive-compulsive disorder (Miller et al., 2019; Kahn et al., 2021). In consequence, the limbic network is often targeted with therapeutic brain stimulation to modulate brain function (Lockman and Fisher, 2009; Miller et al., 2019; Gregg et al., 2021). Although therapeutic effects have been shown with HC and ANT stimulation in particular (Lockman and Fisher, 2009; Lozano et al., 2019; Nair et al., 2020; Gregg et al., 2021; Pal Attia et al., 2021), more sophisticated and precise technology has been emerging that senses brain activity in addition to stimulating the brain. Characterizing stimulation-evoked waveforms would allow detecting typical or pathologic waveforms with such closed-loop systems (Wu et al., 2018).

Characterizing electrophysiological waveforms in the limbic system is relatively challenging with noninvasive electroencephalographic (EEG) or magnetoencephalographic techniques because of its deep location. Stereo EEG (sEEG) electrodes placed during invasive epilepsy monitoring can be used to identify cortical connections of deeper human brain networks (Keller et al., 2014; Enatsu et al., 2015). Direct SPES can be delivered to a particular site while measuring the electrophysiological responses elsewhere (Borchers et al., 2011). Previous studies measuring these corticocortical evoked potentials (CCEPs) have confirmed direct anatomic connections within the limbic network using early responses (Matsumoto et al., 2004; Kubota et al., 2013; Enatsu et al., 2015; Oane et al., 2020).

In this study, we show different stimulation-driven waveforms when delivering to and recording from limbic regions (amygdala, HC, ANT, and cingulate). We assume that evoked waveforms related to anatomic networks (1) have reliable timing and waveform across trials, (2) share the same features across subjects, (3) have reversed polarity across superficial and deep cortical recording sites, indicating a local current source and sink, and (4) stimulating further downstream in a network should elicit evoked potentials that arrive earlier at a recorded end point. Using these criteria, we characterize a distinctive limbic HAP-wave present in HC-ANT-PCC connections, which belong to the hippocampal subsystem of the limbic network.

## Materials and Methods

### Subjects

Data were collected from neurosurgical patients with sEEG probes implanted within the limbic network during invasive epilepsy monitoring. Eight subjects (four males and four females) between 13 and 63 years old (mean, 30 years old; Table 1) provided informed consent to participate in the study, which was approved by the Institutional Review Board of Mayo Clinic. During clinical monitoring, the seizure onset zone (SOZ) and regions with interictal activity were identified by epilepsy neurologists (Table 1). The limbic network was involved in the SOZ only for subject 6 involving a subset of the electrodes in the hippocampus (two of seven electrodes) and posterior cingulate cortex (one of two electrodes), and for subject 8 involving the amygdala contacts and a subset of electrodes in the hippocampus (four of eight electrodes; Table 1, SOZ column).

### Electrode localization and inclusion

Multicontact flexible sEEG probes (DIXI Medical) with electrode contacts 2 mm in length and 0.8 mm in diameter were implanted. Probes had lengths between 16 mm (5 contacts) and 80.5 mm (18 contacts; Fig. 1B). The placement of the sEEG probes was selected by the clinical team for the purpose of SOZ localization, with electrode coverage of different brain regions (Fig. 1A, sEEG schematic) according to the clinical planning.

Electrodes were localized using a computed tomography scan (Hermes et al., 2010) and were aligned to the T1-weighted (T1w) anatomic magnetic resonance imaging (MRI) using existing software (Friston et al., 2007; <https://www.fil.ion.ucl.ac.uk/spm/software/download/>). MRI scans were autosegmented using FreeSurfer 7 (Fischl, 2012; <https://surfer.nmr.mgh.harvard.edu/>). The segmentation was reviewed for accuracy, and sEEG electrodes were labeled according to the FreeSurfer Destrieux Atlas (Destrieux et al., 2010). Electrodes labeled as amygdala, hippocampus, parahippocampal gyrus, thalamus, and cingulate cortex were included in the study. Sites labeled as “anterior cingulate” and “middle anterior cingulate” were grouped together as ACC; and sites labeled as “middle posterior cingulate,” “posterior-dorsal cingulate,” and “posterior-ventral cingulate” were grouped together as PCC. Sites labeled as “hippocampus” and “parahippocampal gyrus” were grouped together as HC (Nemanic et al., 2004). Estimated positions of the electrodes are shown in Extended Data Figures 2-1 and 2-2.

### Electrode depth calculations

To categorize electrode contacts as superficial or deep, we calculated the distances between the electrodes and the gray matter/white matter border estimated in FreeSurfer. Given an average cortical thickness of 2.5 mm (Fischl and Dale, 2000), we considered an electrode with a distance  $>2.3$  mm from the gray matter/white matter border to be superficial, whereas an electrode with a distance  $<2.3$  mm was considered to be deep.

### CCEPs and intracranial EEG measurements

Using a Nicolet Cortical Stimulator (Natus), SPES was delivered using biphasic pulses of 200  $\mu$ s duration. For subjects 1–6 and 8, SPES was applied with 6 mA amplitude by the experimenter every 3–5 s with jitter

**Table 1.** Demographic description of subjects included

Subject	Age	Sex	Hemisphere implanted	Limbic coverage	SOZ	Interictal notes	Treatment plan
Sub-01	30	Female	Right	HC, Amg, ACC, MAC, PDC	Posterior insula/parietal operculum	HC	Resective surgery
Sub-02	19	Male	Right	HC, ACC, MPC, Tha	Mid and posterior insula	HC	Laser ablation
Sub-03	31	Female	Right	HC, Amg, ACC, MAC, MPC	AC, MAC, and mesial superior frontal gyrus	HC, inferior mid-frontal orbital gyrus, superior frontal gyrus, white matter	Resective surgery
Sub-04	13	Female	Left	HC, Amg, ACC, MPC, PDC	Inf-posterior insula	HC, Amg, PDC and medial insula	Laser ablation
Sub-05	46	Male	Right	PHc, Amg, MPC, PDC	Sup-frontal gyrus and sulcus, sup-temporal gyrus and sulcus	PHc, Amg, sup-temporal sulcus, mid-temporal gyrus, mid-temporal lingual gyrus, fusiform gyrus	Implantation of neurostimulator
Sub-06	63	Male	Left	PHc, HC, Amg, PDC, PVC	Anterior and left insula, parieto-temporal region, HC (2 of 7) and PDC contacts	Amg, HC, inf-parietal supramar gyrus, subcentral gyrus and sulcus	Diet and medication adjustment
Sub-07	19	Male	Left	HC, Tha, MAC, ACC, MPC, PDC	Medial and Inferior frontal gyrus and sulcus	Superior, middle, and inferior frontal gyrus, sup-temporal gyrus and HC contacts	Resective surgery
Sub-08	20	Female	Right	HC, Amg, Tha, ACC, MPC, PDC, PVC	Amg, HC, temporal-parietal sulcus and gyrus, occipital-temporal sulcus and gyrus	HC, MPC, PVC, temporal-superior sulcus, parieto-occipital sulcus	N/A

Sub, Subject; PHc, parahippocampal gyrus; MAC, mid-anterior cingulate; MPC, mid-posterior cingulate; PDC, post-dorsal cingulate; PVC, post-ventral cingulate; Tha, thalamus; Inf, inferior; Sup, superior.

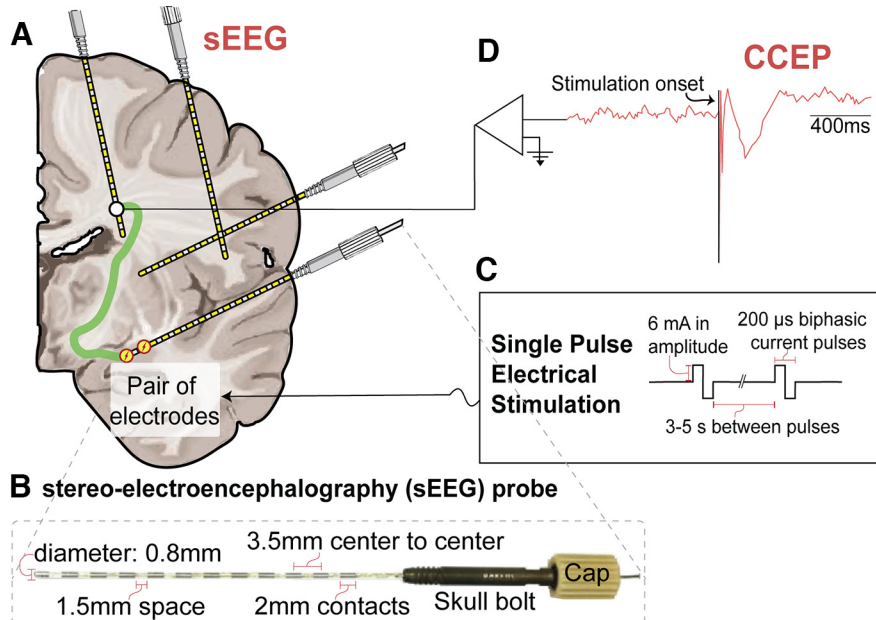


**Figure 1.** Illustration of the CCEPs experimental paradigm. **A**, Schematic of a brain implanted with sEEG probes. Illustration shows a CCEP paradigm where stimulation is delivered and signals are depicted in all the other contacts. **B**, Picture of a 12-contact DIXI Medical MICRODEEP sEEG probe with cap and skull bolt and its dimensions. **C**, Parameters used when delivering single-pulse biphasic electrical stimulation. **D**, Illustrative schematic of the amplified CCEP signal, showing the stimulation onset followed by a classical evoked potential.

for a total number of 10–12 applications (Fig. 1C). In subject 8, one hippocampal pair was stimulated 55 times. With SPES of 6 mA during 200  $\mu$ s through an electrode surface area of 5 mm<sup>2</sup> (length, 2 mm; diameter, 0.8 mm; Fig. 1B), a charge density of 24  $\mu$ C/cm<sup>2</sup> was calculated, which is below the safety charge density limit (30  $\mu$ C/cm<sup>2</sup>; Cogan et al., 2016). Given the higher excitability observed in subject 7, lower amplitudes of 3 and 4 mA were used for most sites, with charge densities of 12 and 16  $\mu$ C/cm<sup>2</sup>, respectively. CCEPs were recorded (Fig. 1D) at 2048 Hz using a Quantum Amplifier (Natus).

#### Data preprocessing

As part of the data curation process, channels that had excessive noise or were positioned at the end of the sEEG probe located outside of the brain were marked as bad and excluded from analyses. On average, 12% of contacts were excluded across subjects (range, 5–18%). CCEP recordings were visually inspected and labeled for electrical and movement artifacts, excluding those channels and trials with excessive line noise or artifacts. We consider one trial to be the response recorded after an individual

SPES (from 0 to 2 s after the stimulation onset). We then rereference the data using an adjusted common average referencing (CAR) scheme, because local reference schemes (e.g., bipolar referencing) can affect the polarity of the response, and a regular common average may introduce bias if many electrodes show a large response. As previous studies have suggested including only those channels with lower variance (Uher et al., 2020; Mercier et al., 2022), we rereferenced the data to an adjusted CAR scheme where the common reference is based on the 20% of channels with the lowest variance. Additionally, we consider the fact that in our data noise was shared across blocks of 64 channels, because 64 channels were acquired within 1 headbox (maximum, 4 headboxes; total, 256 channels). Therefore, for each channel, we consider the 64 channels from the same headbox to calculate a common reference after we exclude (1) the stimulated channels, (2) channels labeled as bad, and (3) the 80% of channels with the largest variance from 15 to 500 ms after stimulation. This adjusted common average reference signal was then subtracted from all other channels within the same 64-channel block. The

start time of 15 ms was used to exclude the influence of stimulation artifacts. Stimulation artifacts can potentially spread to nearby electrodes through volume conduction and the following helped ensure that this did not affect our results. First, volume conduction effects are largest in the first 1–8 ms after electrical stimulation (Trebau et al., 2016), and responses were only detected after 15 ms. Second, we look at long distance connections, and our findings between hippocampus or amygdala and cingulate cortex exclude electrodes within 13 mm from the stimulated electrode pair, at which distances the effects of volume conduction are largely negligible (Prime et al., 2020). A baseline correction was used by subtracting the median amplitude from 0.5 to 0.05 s before each stimulation from each trial.

#### Statistical analyses

**CCEP waveform significance and reliability.** To identify stimulation-driven signatures in the limbic system, we aim to characterize significant CCEPs that have a reliable waveform across trials. To determine these significant CCEPs, we use canonical response parameterization (CRP; Miller et al., 2023). This method is based on cross-trial projections to extract CCEP responses that have a reliable morphology across trials. The advantage of CRP is that it allows for different brain areas with dissimilar trace shapes to be directly compared, and CRP establishes statistical significance and provides the explained variance as a measure of response reliability. In brief, electrodes were stimulated  $K$  times, with  $K = 10–55$ , resulting in matrix  $V$  with dimensions  $T \times K$  with  $T$  as the total number of timepoints and  $K$  as the total number of trials. A cross-projection matrix,  $P$ , was calculated for each stimulation electrode pair as scalar projections between all pairs of trials from 15 to 1000 ms, with self-projections removed:  $P = \hat{V}^T V$ , where  $\hat{V}_k(t) = V_k(t)/|V_k(t)|$  is unit normalized for each trial. The full matrix  $P$  is sorted into a combined set  $S$  with self-projections omitted. For each measured electrode and stimulation pair,  $S$  provides a distribution of cross-projection magnitudes across trials, and the average of the set of cross-projections,  $\bar{S}$ , summarizes the interaction from stimulation to response. When this cross-projection matrix is calculated for increasing trial length (15–1000 ms), we can quantify the temporal profile  $\bar{S}_t$ . Because  $S$  can be thought of as a measure for mutual information between trials, the peak of  $\bar{S}_t$  represents the time past for which further information is not reliable. This peak time is therefore considered the response duration  $\tau_R$ . The distribution of the cross-projection magnitudes at the response duration  $\bar{S}_{\tau_R}$  across the different trials can be tested for significance to indicate that there is a significant CCEP waveform where  $\bar{S}_{\tau_R} > 0$  using a right-tailed  $t$  test. Using this CRP method (see Miller et al., 2023 for full details), we thus test whether CCEPs in the limbic network are significant, and we correct the CRP-based  $p$  value for multiple comparisons using a false discovery rate (FDR) correction per the Benjamini and Yekutieli (2001) method. The advantage is that this CRP method fully depends on intertrial reliability, while not depending on the shape of the CCEP, and no prior assumptions are made for response duration or polarity.

To quantify the reliability of a connection, the CRP method provides the explained variance  $R^2$  in the evoked response for each trial  $K$  [ $V_k(t)$ , truncated to time  $\tau_R$ ] explained by the canonical response  $\alpha C(t)$ . The  $R^2$  is calculated for each trial  $K$  as follows:

$$\begin{aligned} R^2 &= 1 - \frac{SS_{\text{res}}}{SS_{\text{total}}} \quad \text{with } SS_{\text{res}} = \sum_t (V_t - \alpha C_t)^2 \text{ and } SS_{\text{total}} \\ &= \sum_t (V_t - \bar{V})^2. \end{aligned}$$

The median  $R^2$  across trials provides an estimate for the reliability of the CCEP that is well interpretable and has units of proportion-explained variance.

**Early response detection.** After identifying significant responses without prior assumptions on their waveform with the CRP method, we calculate which percentage of these waveforms shows an early response. Many previous reports have focused on these early responses within

~50 ms of stimulation onset as they have been related to more direct connections between stimulated and measured areas (Matsumoto et al., 2004; Keller et al., 2014; van Blooij et al., 2023). Whereas electrocorticographic brain surface recordings generally focus on N1, the polarity of an early response can be either positive or negative in sEEG recordings dependent on their laminar position (Prime et al., 2018; Huang et al., 2023). We detected early responses in the same way as previously (van Blooij et al., 2023). Peaks are first detected from 15 and 50 ms poststimulation in the average CCEP waveform. A peak was considered an early response, when the amplitude exceeded 3.4 times the SD during the baseline period from 500 to 20 ms before stimulus onset.

**Linear mixed-effects model to compare intranetwork versus internetwork responses.** If limbic subsystems have stronger in-network connections, we expect that in-network responses are more reliable compared with cross-network responses. Specifically, we expect that connections from the hippocampus to PCC and amygdala to ACC are more reliable compared with connections from hippocampus to ACC or amygdala to PCC. To test for this, we use the CRP method-based explained variance ( $R^2$ ) in a linear mixed-effects model to compare intranetwork versus internetwork response reliability.

The linear mixed-effects model can be designed in several ways, as follows: Model 1, with a random intercept; Model 2, with an independent random intercept and slope; or Model 3, with a random intercept and slope with correlation between them. We first fit Model 1 and then add complexity by comparing Model 2 versus Model 1 and Model 3 versus Model 2. To compare models, we use the simulated theoretical likelihood ratio test with 1000 replications (using the MATLAB *compare* function). This comparison takes the explained variance into account with a penalty for model complexity.

We first fit the linear mixed-effects Model 1 with stimulation site (HC or amygdala) and measurement site (PCC or ACC) as categorical fixed effects and subject as a random effect on the intercept (using the MATLAB *fitlme* function) to the  $R^2$ . Model 1 with only a random intercept is represented by the following equation:

$$\begin{aligned} y_{ij} &= \beta_0 + \beta_1 \text{stimulationSite} + \beta_2 \text{measurementSite} \\ &\quad + \beta_3 (\text{stimulationSite} * \text{measurementSite}) + b_i + \varepsilon_{ij}, \end{aligned}$$

where  $y_{ij}$  denotes the  $R^2$  for the  $j$ th CCEP (CCEP related to 1 measured electrode and 1 stimulated pair) in the  $i$ th subject. The coefficient  $\beta_0$  represents the intercept term, while  $\beta_1$  and  $\beta_2$  represent the fixed-effect coefficients for the measurement site and stimulation site, respectively. Additionally,  $\beta_3$  represents the coefficient for the interaction term between the measurement site and stimulation site. The subject-specific random effect was accounted for by the term  $b_i$ , capturing individual variability. The residual term,  $\varepsilon_{ij}$ , accounted for the unexplained variability or random error. This model allowed us to assess the effects of measurement site, stimulation site, and their interaction on the reliability of the CCEP ( $R^2$ ). After evaluating the linear mixed-effects model by maximum likelihood, we use the Satterthwaite approximation for the degrees of freedom of the  $F$  test, which has been reported to properly control for type 1 error for small sample sizes (Luke, 2017).

**Time lag between inputs from different sites.** In the limbic circuit, the PCC is connected to the HC and ANT. To understand whether PCC responses to HC and ANT stimulation were similar, but lagged in time, we calculated time-lagged cross-correlations between HC and ANT evoked responses in PCC within two subjects that had electrodes placed in all three areas. Cross-correlations were calculated among all trials with PCC responses when the HC was stimulated ( $n$  trials) and when ANT was stimulated ( $m$  trials), resulting in  $m \times n$  cross-correlations. To calculate confidence intervals of the cross-correlation and time lag between the two inputs, we used a bootstrapping method (Efron and Tibshirani, 1998) and sampled with replacement 10,000 times from observed cross-correlations to estimate the time lag between the responses measured in PCC while stimulating HC or ANT.

**Wavelet principal component analysis and linear discriminant analysis.** To quantitatively assess the difference in waveform morphology in limbic subsystems across subjects, we test whether we can discriminate

the waveforms in ACC and PCC after stimulating the amygdala and HC using a linear discriminant analysis (LDA). Principal component analysis (PCA) was performed in the discrete wavelet domain on significant CCEPs between limbic regions to provide a low-dimensional visualization of dissimilarity/similarity between tested limbic connections. First, the significant waveforms between limbic regions were L2-normalized between 100 and 500 ms poststimulation. Significant waveforms measured in the PCC were inverted (multiplied by  $-1$ ) if they were positioned in superficial layers based on their electrode depth (see Materials and Methods, subsection Electrode depth calculations). Then, the highest-level (8) discrete wavelet transform of each waveform was calculated using the fourth Symlet wavelet, and all coefficients below the 95th percentile were set to 0 to only maintain the largest coefficients (see Fig. 8A). The wavelet transformation and thresholding steps allow transient, large-amplitude changes in the signal to be emphasized while reducing low-amplitude noise, regardless of frequency (Daubechies, 1992; Gupta and Jacobson, 2006; Puyati et al., 2006; Brunton and Kutz, 2022). The set of all transformed waveforms was mean centered at each wavelet coefficient and principal components were determined by singular value decomposition. Waveforms were projected to the second and third principal components, which each independently showed the greatest separation between the amygdala-to-ACC and HC-to-PCC conditions of the first five principal components, as quantified by the *t*-statistic. LDA was performed in this two-dimensional space between those two limbic conditions. LDA model accuracy was assessed using leave-one-subject-out cross-validation, where the wavelet-transformed waveforms from each test subject were withheld before PCA and then projected onto the principal components calculated from the training fold (waveforms in the remaining six subjects) for classification. Statistical significance was determined by permutation testing: a null accuracy distribution was estimated for each left-out subject by randomly permuting all waveform labels within each subject before LDA model training and testing, repeated for 100,000 permutations. The prediction accuracy for each left-out subject was deemed significantly above chance if it lay in the right tail of the null distribution, at an FDR of 0.05 (Benjamini and Yekutieli, 2001). The statistical significance for the mean cross-validation accuracy was determined similarly by comparison with the mean accuracy across left-out subjects at each permutation of the null model.

We compared the cross-validation accuracy of the above LDA model to the cross-validation accuracies of LDA models trained and tested more simply on principal components of time domain waveforms. The following seven filtering conditions were tested: unfiltered; low-pass filtered at 4, 8, and 13 Hz (to mitigate high-frequency noise); and bandpass filtered within the canonical frequency bands  $\theta$  (4–8 Hz),  $\alpha$  (8–13 Hz), and  $\beta$  (13–30 Hz). For each condition, the same significant limbic waveforms as above were first L2 normalized by the magnitude between 100 and 500 ms poststimulation, but a longer interval between 15 and 1500 ms was kept before filtering to avoid edge effects. The start time of 15 ms also excluded sharp transient stimulation artifacts. The waveforms were subject to forward-reverse filtering (MATLAB *filtfilt*) using a fourth-order low-pass filter or a fourth-order bandpass Butterworth filter, depending on filtering condition, and then clipped between 100 and 500 ms. Principal components were calculated in the same way as above from the filtered time domain waveforms, and all waveforms were projected to the two principal components, of the first five, that independently showed greatest separation between the amygdala-to-ACC and hippocampus-to-PCC conditions as quantified by the *t*-statistic. Cross-validation accuracy was calculated in the same way as for the above LDA model.

#### *Diffusion-weighted imaging and tractography*

Subjects 2 and 7 were scanned in a Compact 3.0 T MRI scanner with high-performance gradients (Foo et al., 2018) at Mayo Clinic Rochester under an institutional review board-approved protocol. We used Distortion-free imaging: a double-encoding method (In et al., 2020) to scan two series with each two volumes at  $b = 0 \text{ s/mm}^2$  and 48 directions at  $b = 1000 \text{ s/mm}^2$ , TR = 2659 ms; TE = 42.7 ms; TE<sub>NE</sub> = 49.6 ms (TE<sub>NE</sub> is navigator echo time for the DIADEM sequence), 70 slices at 2

mm thickness (zero gap), FOV of 216 mm, and acquisition matrix of 108  $\times$  108.

Diffusion MRI (dMRI) data were preprocessed to correct for subject motion and eddy currents and to align the dMRI images and T1w anatomic image using the Advanced Normalization Tools algorithm in QSIprep version 0.14.2 (Cieslak et al., 2021). QSIprep includes denoising using *dwidenoise* in MRtrix3 to improve the signal-to-noise ratio and to increase the accuracy of the diffusion parameter estimation and a B1 Bias Field Correction using ANTs/MRtrix3 *dwibiascorrect* to correct for any inhomogeneity in the radio frequency field.

DSI studio was used to track different subcomponents of the cingulum bundles and the fornix (fx) bundles. First, the restricted diffusion was quantified using restricted diffusion imaging (Yeh et al., 2017). Next, the diffusion data were reconstructed using generalized q-sampling imaging (Yeh et al., 2010) with a diffusion sampling length ratio of 1.25. Finally, a deterministic fiber tracking algorithm (Yeh et al., 2013) was used with augmented tracking strategies (Yeh, 2020) to improve reproducibility. The anatomy prior of a tractography atlas (Yeh et al., 2018) was used to map the fornix and cingulum bundles with a distance tolerance of 16 mm. The anisotropy threshold was randomly selected, the angular threshold was randomly selected from 15° to 90°, and the step size was randomly selected from 0.5 to 1.5 voxels. Tracks with lengths <20 mm or >300 mm were discarded. A total of 5000 tracts were calculated. Topology-informed pruning (Yeh et al., 2019) was applied to the tractography with 12 iteration(s) to remove false connections.

#### *Data availability*

Code was written in MATLAB to reproduce the statistics and figures contained in this article and is available on our GitHub page <https://github.com/MultimodalNeuroimagingLab/HAPwave>. Data are shared in BIDS (Brain Imaging Data Structure) format on OpenNeuro.org, <https://openneuro.org/datasets/ds004696>.

## Results

To understand whether limbic subsystems have distinct stimulation-evoked network signatures, we stimulate and measure from different limbic regions. We first visualize the significant CCEP waveforms across subjects (Fig. 2) revealing many different responses in addition to early responses. Second, we show that the CCEP from HC to the PCC (HC-to-PCC) displays a characteristic waveform across trials in two subjects, with a characteristic peak at 200 ms, which we will call the “limbic HAP-wave” (Fig. 3). Third, we show that the limbic HAP-wave from HC-to-PCC is observed across all subjects and show that the reliability of the waveforms from HC-to-PCC is higher than that from the amygdala-to-PCC, which was not the case in ACC, further establishing the strength of connectivity within limbic subsystems of HC-to-PCC and amygdala-to-ACC (Fig. 4). Fourth, to confirm the current source and sink of the limbic HAP-wave peak at 200 ms in the PCC, we show that the peak is typically reversed at deep and superficial PCC recording sites (Fig. 5). Fifth, we show that stimulating more posterior in the HC evokes faster responses in the PCC (Fig. 6). Sixth, since a 200 ms delay is too long for a direct connection, we further probe the network involved in these PCC waveforms by stimulating the ANT and extracting the white matter bundles potentially involved in the propagation of the waveform in two subjects (Fig. 7). Last, we test whether waveforms measured in limbic subsystems, from amygdala to ACC versus HC to PCC could be discriminated (see Fig. 8).

#### **Limbic network waveforms across subjects**

First, we visualize the stimulation-evoked network waveforms of the different limbic connections across all subjects. Electrodes

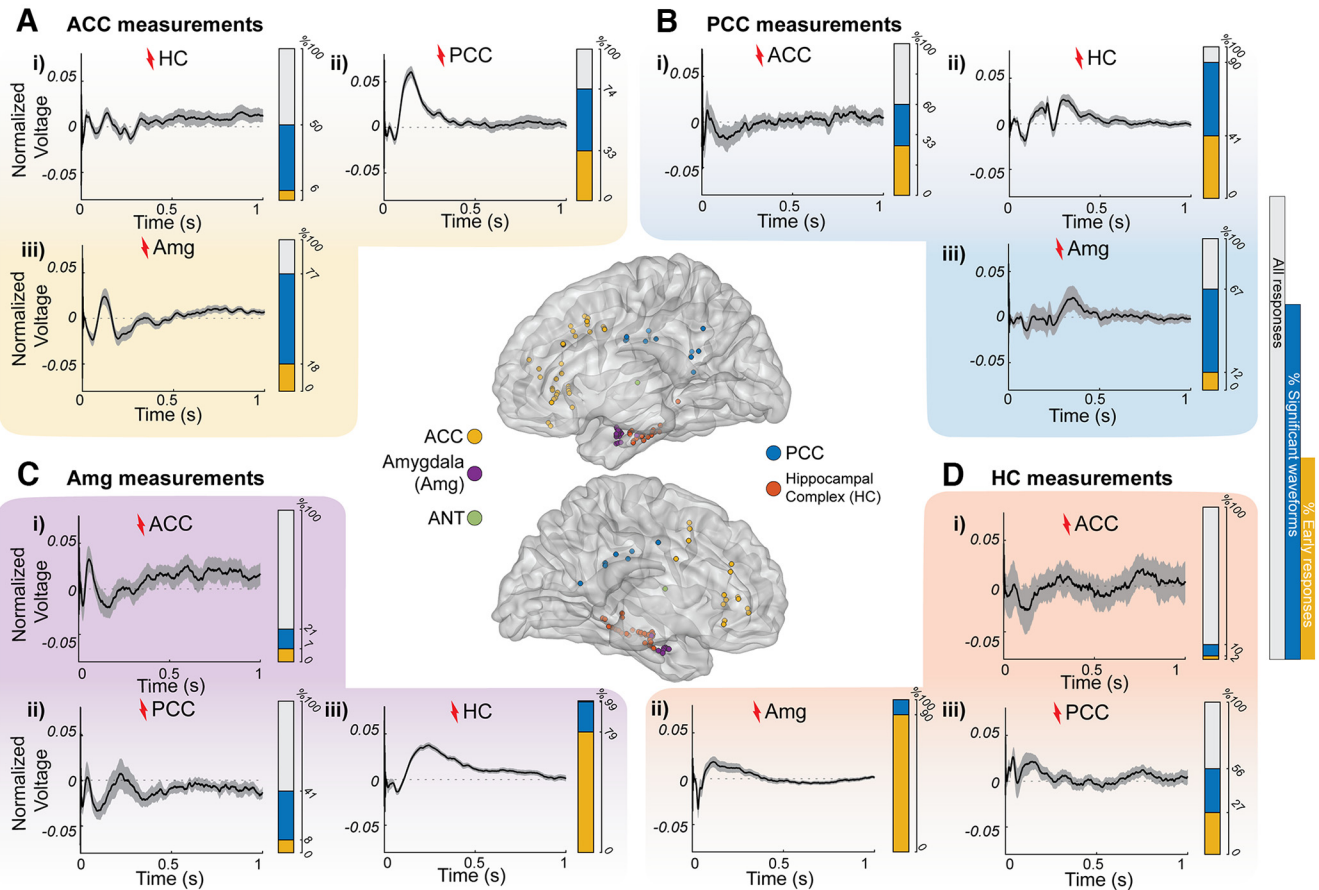


**Figure 2.** Stimulation-driven waveforms in limbic connections across subjects. **Ai–Diii**, MNI brain renderings of right (top) and left (bottom) hemispheres with the electrode sites where the signals shown were measured and stimulated. Extended Data Figures 2-1 and 2-2 show the coverage in individual subjects. The average of all significant L2-normalized CCEPs (thicker black line) plotted over time with a 95% confidence interval (gray shadow) is shown. **Ai–iii**, Measurements in the ACC after HC (*i*), PCC (*ii*), and amygdala (*iii*) stimulation. **Bi–iii**, Measurements in the PCC after ACC (*i*), HC (*ii*), and amygdala (*iii*) stimulation. **Ci–iii**, Measurements in the amygdala after ACC (*i*), PCC (*ii*), and HC (*iii*) stimulation. **Di–iii**, Measurements in the HC after ACC (*i*), amygdala (*ii*), and PCC (*iii*) stimulation. Extended Data Figures 2-3 and 2-4 show normalized responses in individual subjects of direct HC–Amg connections. Additionally, each panel contains a bar representing overlays of all CCEP connections (gray) with the percentage of significant responses (blue, based on CRP method cross-trial reliability) and significant responses with a significant early response from 15 to 50 ms (yellow portion).

were placed in HC, Amg, PCC, ACC, and ANT [Fig. 2, middle, electrode positions in a standard brain (MNI152), Extended Data Figs. 2-1, 2-2, coverage in individual subjects]. Figure 2 shows the CCEP waveforms averaged across the significant responses across all subjects, as follows: responses were considered significant when cross-trial projections are significantly  $>0$  ( $p_{\text{FDRcorrected}} < 0.05$ ; see Materials and Methods; Miller et al., 2023), indicating highly reliable waveforms across trials. As this method depends on cross-trial reliability and is independent of a specific waveform, it allows us to observe the broad range of stimulation-driven waveforms throughout the limbic network.

These significant responses in the limbic network show many different shapes, and classical early responses (e.g., an N1) were not always present. For all the significant responses, we detected the presence of an early response within 50 ms after stimulation (either positive or negative given the sEEG recordings at different cortical depths). When stimulating and measuring adjacent sites (PCC–ACC or HC–amygdala), many connections contain the classical early responses (33–90%; Fig. 2Aii, Bi, Ci, Dii, Extended Data Figs. 2-3, 2-4, normalized responses in individual subjects). For the long-range connections between distant sites

(HC/amygdala  $\leftrightarrow$  PCC/ACC), only smaller percentages contain early responses (2–41%; Fig. 2Ai, Aiii, Bii, Biii, Ci, Cii, Di, Diii).

These long-range connections show many other waveforms. Measurements in the ACC show that 77% of responses are significant after amygdala stimulation, showing large-amplitude waveforms lasting up to 500 ms, but only 18% show an early response (Fig. 2A). Measurements in the PCC show that 90% of responses are significant after HC stimulation, but only 41% show an early response (Fig. 2B). Surprisingly, these HC-to-PCC responses show a sharp peak at  $\sim$ 200 ms, a much later response than the early latencies typically reported within the first 50 ms after stimulation. Measurements in amygdala (Fig. 2C) show some significant responses across the subjects from ACC or PCC stimulation (respectively, 21% and 41% of all responses are significant and only 7% and 8% show an early response). Measurements in HC, however, show 56% significant responses from PCC stimulation (27% of all responses had an early response), but only 10% of responses are significant after ACC stimulation (2% of all responses have an early response). These data emphasize the strong inputs from HC-to-PCC or amygdala-to-ACC. The waveforms of these responses may be better appreciated at the

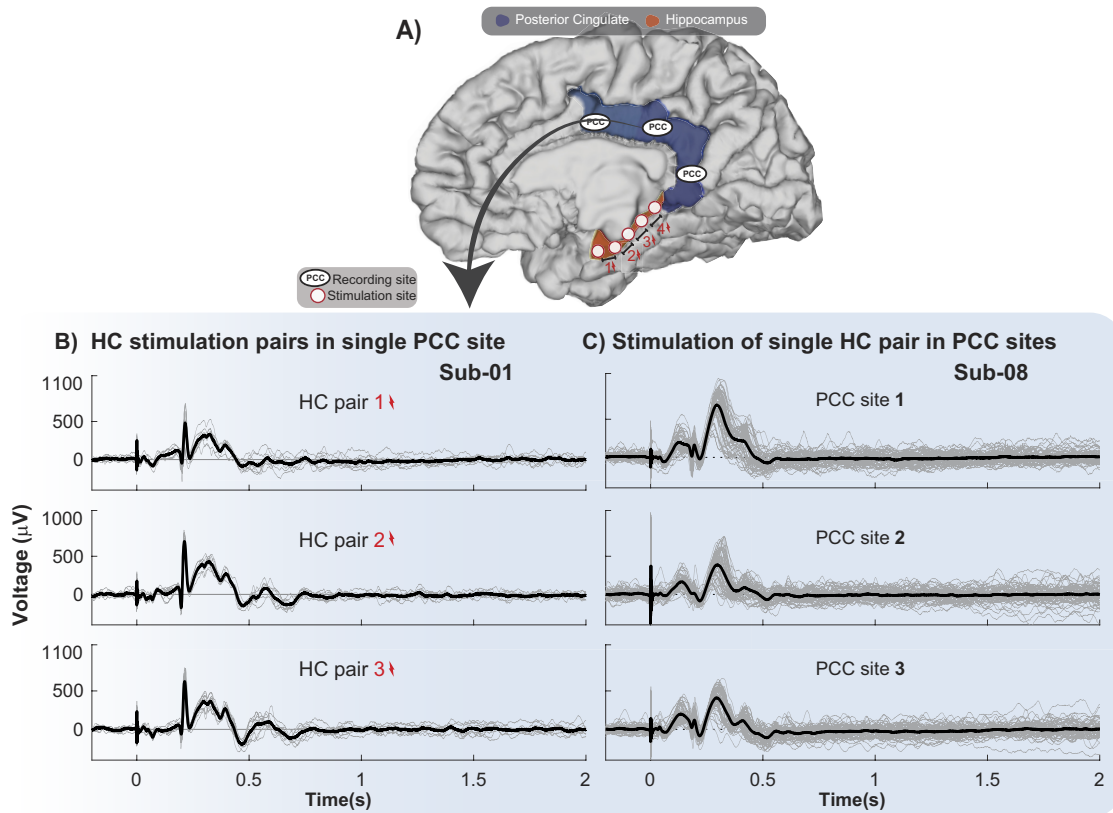


**Figure 3.** Significant PCC CCEP waveforms are reliable when stimulating along the HC and recording in the PCC across trials. **A**, Brain schematic with representative recording and stimulation sites, with PCC (blue) and outline of the hippocampal complex HC (orange), since hippocampus is located underneath the cortical surface. **B**, **C**, Individual CCEP trials ( $\mu$ V; gray lines) and average response (black line) after stimulating HC electrodes denoted in two different subjects. Stimulation onset is at time 0. **B**, CCEP waveforms from a single contact in PCC in subject 1 (Sub-01) after stimulating different pairs of electrodes in the HC 10 times. **C**, CCEP waveforms from different contacts in the PCC in subject 8 (Sub-08) after stimulation of a single HC pair of electrodes 55 times.

single-subject and trial levels, as the averaging across subjects may obscure some of the details in the waveforms.

#### Long-latency CCEP in PCC after HC stimulation: limbic HAP-wave

To appreciate the waveform of the significant long latency responses in the HC-to-PCC connection, we show single-trial data from subjects 1 and 8 (Fig. 3). After stimulating different pairs of electrodes located along the HC 10 times, we analyze the data from a single PCC site (Fig. 3B, subject 1) and after stimulating one pair of electrodes in the HC 55 times, we analyze the data across several PCC sites (Fig. 3C, subject 8). This example shows the prominent and consistent CCEPs in the PCC when stimulating along HC electrode pairs (Fig. 3B). Individual trials show a sharp peak at  $\sim$ 200 ms, which is often preceded and followed by slow positive waves until  $\sim$ 500 ms. Thus, we confirm that this unique waveform is reliable across trials and is not driven by outliers or fluctuating interictal activity. We will further refer to this waveform as the limbic HAP-wave.

This limbic HAP-wave is a common feature in most HC-to-PCC connections across subjects. Figure 4 shows that stimulation in HC often evokes a sharp peak at  $\sim$ 200 ms in the PCC (Fig. 4D, Extended Data Fig. 4-1, similarities in morphology on normalized waveforms). Although a similar peak at 200 ms can be present in other connections, such as the amygdala-to-PCC, Figure 4D shows that the limbic HAP-wave peak is typically larger in amplitude in the HC-to-PCC connection. This waveform is not clear in subject 7, but we note that

stimulation amplitude was reduced in subject 7. The limbic HAP-wave is often positive in polarity with a total duration of  $\sim$ 500 ms. Differences in polarity and latency will be addressed in subsequent Figures 5 and 6.

#### Limbic subsystems have reliable connections

The long-range connections from HC-to-PCC and amygdala-to-ACC have been related to different subsystems in the limbic network involved in memory and emotion respectively. If the waveforms in this study are related to these subsystems, we expect that there will be an interaction between stimulating in HC and amygdala and measuring in PCC and ACC; responses in PCC should be more reliable with HC compared with amygdala stimulation, and responses in ACC should be less reliable with HC compared with amygdala stimulation. To test for this interaction, we use a linear mixed-effects model to test the reliability ( $R^2$ ) of all CCEPs (whether significant or not) with stimulation and measurement site as fixed effects while controlling for subjects as a random effect. The linear mixed-effects model that described the data best was a model with a random intercept and slope, without interactions between these. This model explained the data significantly better compared with a model without a random slope (likelihood ratio test,  $p < 0.001$ ) and adding a correlation between the intercept and slope did not significantly explain more variance in the data (likelihood ratio test,  $p = 0.808$ ).

The linear mixed-effects model shows a significant interaction in the reliability (proportion of explained variance  $R^2$ ) of the

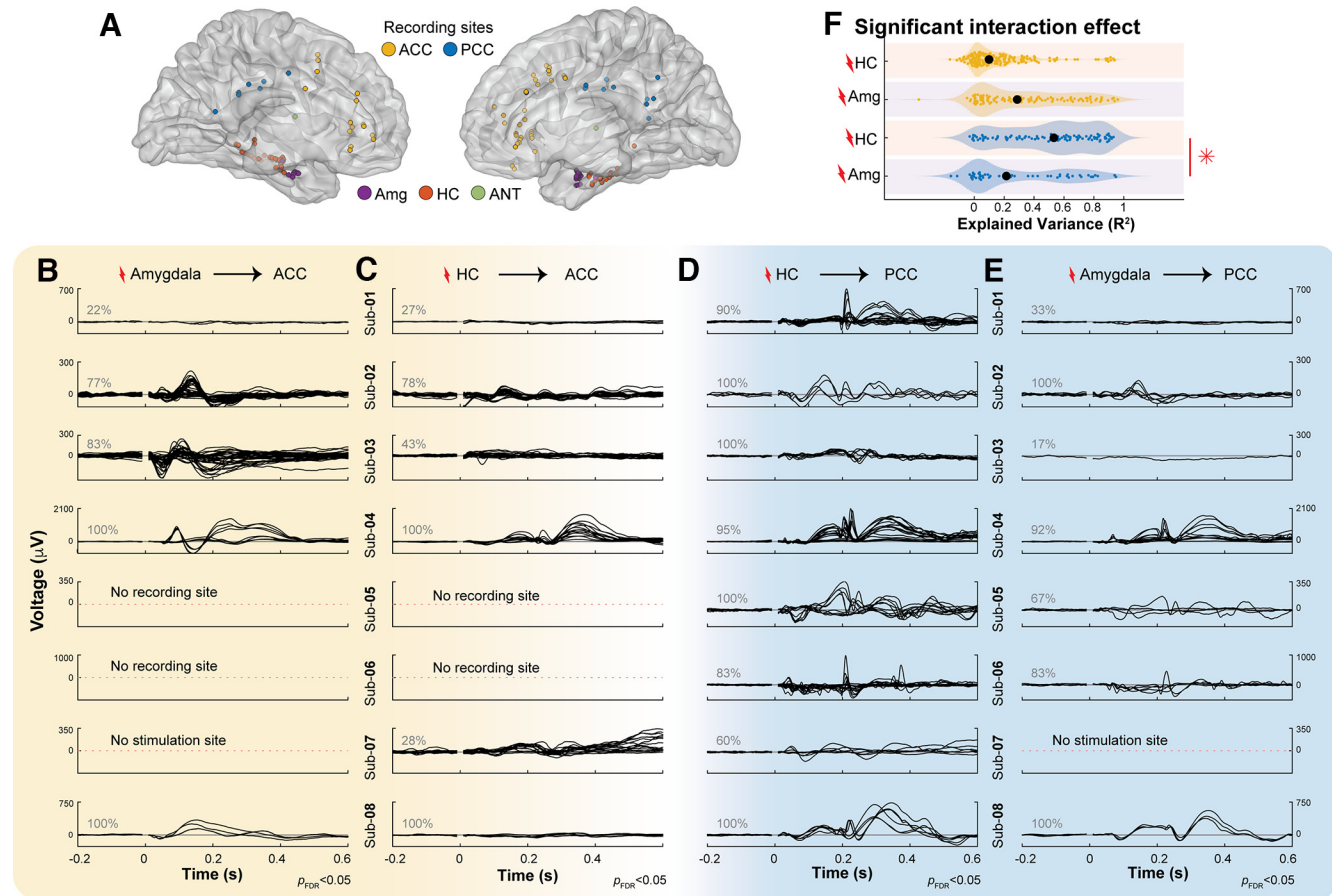


**Figure 4.** Waveforms measured from ACC and PCC during amygdala and HC stimulation. **A**, MNI brain with electrode positions in the Amg (purple circles), HC (orange circles), ACC (yellow circles), and PCC (blue circles). **B**, Significant CCEP waveforms (CRP method-based  $t$  test on cross-trial projections,  $p_{FDR} < 0.05$ ) where the black line shows the average CCEP recorded from an ACC site when stimulating an Amg electrode pair. Gray numbers indicate the percentage of significant CCEPs in each subject. **C**, Same as **B**, recording in ACC, stimulating HC. **D**, Same as **B**, recording in PCC, stimulating HC. **E**, Same as **B**, recording in PCC, stimulating Amg. Extended Data Figure 4-1 shows normalized waveforms. **F**, The proportion of explained variance in the PCC and ACC during HC and Amg stimulation ( $R^2$ , x-axis) was fit by a linear mixed-effects model (see Materials and Methods) with stimulation site (HC and Amg, y-axis) and measured site (ACC, yellow plots; PCC, blue plots) as categorical fixed effects and subject as a random effect. There was a significant interaction effect, and follow-up analyses showed that there were significant differences between the explained variance in the PCC when stimulating in HC or Amg, indicated by a red \*.

CCEP measured in PCC and ACC when stimulating in HC or amygdala ( $F_{(1,6.589)} = 10.96$ ,  $p = 0.014$ , Satterthwaite adjusted; Fig. 4F). Further linear mixed-effects analysis shows that in the PCC, stimulation of the HC elicits responses of increased reliability ( $R^2 = 0.53$ ) compared with the amygdala ( $R^2 = 0.22$ ,  $F_{(1,6.905)} = 11.644$ ,  $p = 0.011$ , Satterthwaite adjusted). This was different in the ACC, where waveform reliability after stimulation of HC ( $R^2 = 0.10$ ) and amygdala ( $R^2 = 0.29$ ) do not differ significantly ( $F_{(1,5.017)} = 2.411$ ,  $p = 0.181$ , Satterthwaite adjusted). Limbic subsystems differ in the reliability of responses, with the memory and spatial subsystem being marked by highly reliable inputs from HC-to-PCC.

#### Polarity of limbic HAP-wave reverses at PCC end points

Polarity reversals between contacts recording from a superficial and a deep source across the cortical surface indicate that there is a signals source between the contacts (Mitzdorf, 1985). We observe that HC-to-PCC connections often elicited a limbic HAP-wave with a sharp peak at  $\sim 200$  ms and an overall latency of  $\sim 500$  ms. However, the peak could be either positive or negative (Fig. 4C). We hypothesize that the variability in polarity is a result of sEEG electrodes recording from different cortical depths. Therefore, we inspect the signals from subjects 1, 3, and

5 where electrodes were placed both relatively superficially, at  $>2.3$  mm from the gray matter/white matter boundary, and deeper in the gray matter ( $<2.3$  mm from the gray matter/white matter boundary). Figure 5A shows the limbic HAP-wave from these different measurement electrodes in the PCC. Differences in polarity are observed in signals recorded from superficial sites (Fig. 5A, dark and light blue traces, B, blue circles represent electrodes) compared with signals depicted deeper in the gray matter ( $\sim 3.5$  mm center to center; Fig. 5A, dark and bright yellow traces, B, yellow circles represent electrodes). The superficial recordings show a peak with negative polarity of  $\sim 200$  ms, whereas the deeper recordings show a peak with positive polarity. These visual inspections help assure that the limbic HAP-wave has a local source and sink in the PCC and do not spread from another area by volume conduction.

#### Variability in latency of responses

We observe that HC-to-PCC connections often elicited a limbic HAP-wave with a sharp peak at  $\sim 200$  ms, but the timing differed between stimulation and recording pairs, particularly in subjects 4 and 8 (Fig. 4D). We hypothesize that the variability in timing in these cases may be related to sEEG electrodes positioned at different distances, as some signals travel further than others. In

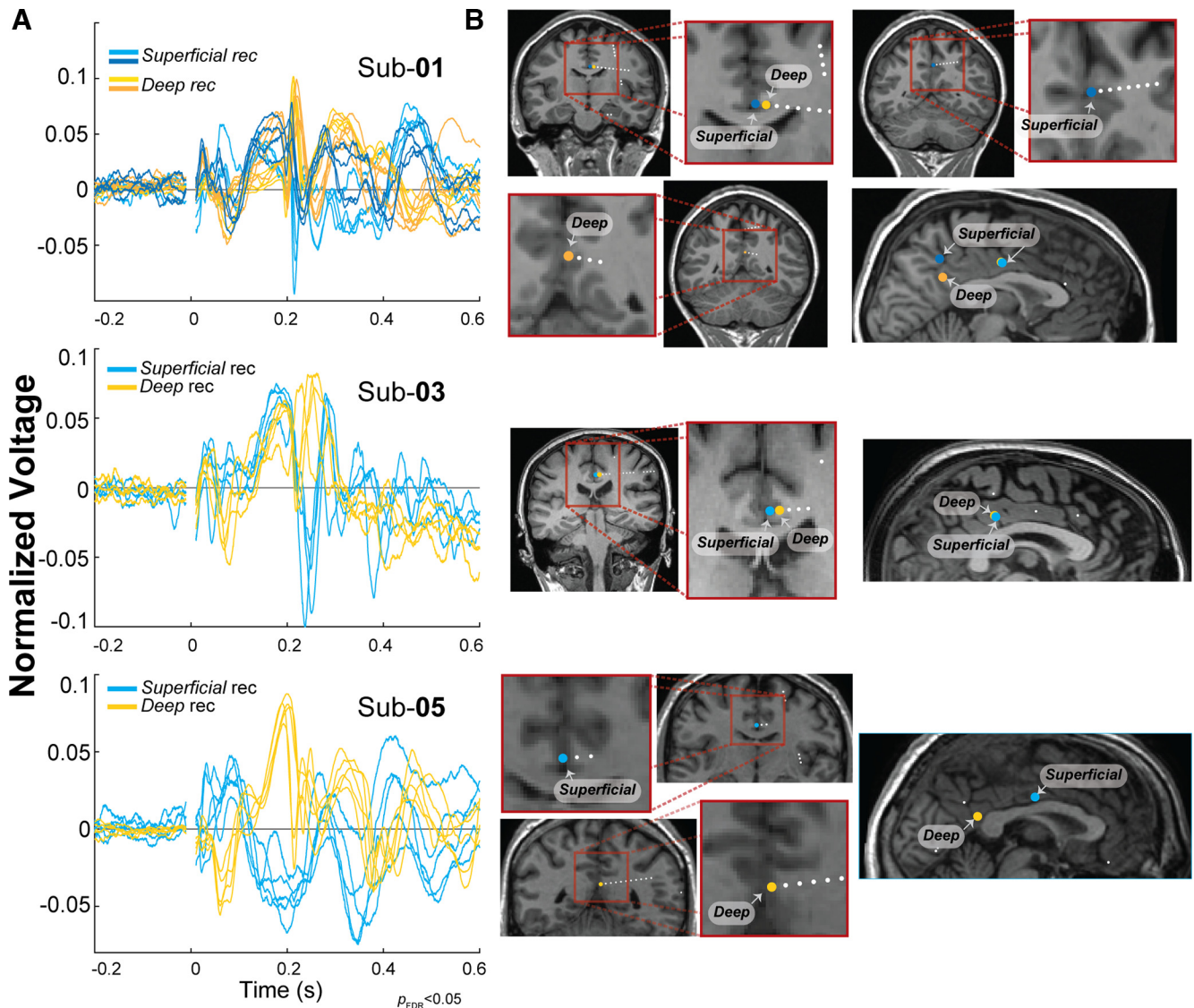


**Figure 5.** Electrodes positioned in different depths of the PCC and variability in morphology. Based on the distance between the electrode and the gray matter/white matter border, contacts were classified as superficial recording (rec) (distance  $>2.3$  mm gray matter/white matter border) or deep (distance  $<2.3$  mm gray matter/white matter border). **A**, Normalized limbic HAP-waves (L2 normalized) from superficial electrodes (blue traces) and deep electrodes (yellow traces) recorded in the PCC on HC stimulation plotted over time. **B**, Coronal view (left) and sagittal view (right) showing an estimation of the superficial (blue circles) and deep (yellow circles) electrode positions for subject 1 (Sub-01), subject 3 (Sub-03), and subject 5 (Sub-05).

subjects 4 and 8, we group together limbic HAP-waves elicited by single sEEG probes within the HC, ending up with a posterior group (Probe I; Fig. 6B, green circles) and an anterior group (Probe II; Fig. 6B, magenta circles), and visualize the limbic HAP-waves in different colors (Fig. 6A, green for posterior stimulation, magenta for anterior stimulation). Stimulation in more posterior HC sites elicits earlier peaks (Fig. 6A, green traces) than stimulation of more anterior HC sites (Fig. 6A, magenta traces).

We note that responses from stimulation of more posterior HC sites are  $\sim 25$  ms earlier compared with sites that are 1 or 2 cm more anterior. This difference in latency is unlikely to be related only to the distance along the fornix, given that typical white matter transmission speeds are much faster than 40 cm/s (Innocenti et al., 2014). However, the longitudinal axis of the hippocampus contains different subfields (Strange et al., 2014), which may play a role as well. This variability in latencies suggests that signals from the HC-to-PCC spread in an anterior-to-posterior direction along the HC (corresponding to a ventral-to-dorsal axis in rodents; Strange et al., 2014).

#### ANT stimulation elicits similar PCC waveforms with reduced latencies

dMRI has delineated several subsegments of the cingulum bundle. There are two possible pathways from the HC to the PCC, the posterior and the anterior. The posterior, connecting through the parahippocampal cingulum bundle ( $ph_{cin}$ ; Fig. 7A, orange tract; Jones et al., 2013; Wu et al., 2016), and the anterior, connecting through the thalamic portion of the limbic system, where hippocampus projects through the fx, to the MBs, which project through the mammillothalamic tract (Grewal et al., 2018) to the ANT, which further projects to the PCC through the parolfactory cingulum ( $po_{cin}$ ) bundle (Mufson and Pandya, 1984; Jones et al., 2013; Wu et al., 2016; Wang et al., 2020; Gregg et al., 2021; Aggleton et al., 2022). The DSI-Studio Software Tool can separately estimate different subsegments of the cingulum bundle (Wu et al., 2016). Figure 7A shows two subjects with electrodes in the HC, ANT, and PCC (Fig. 7, white circles) with the estimates of the fornix, as well as the following different cingulum subsegments: the frontoparietal cingulum ( $fp_{cin}$ ); yellow tract),

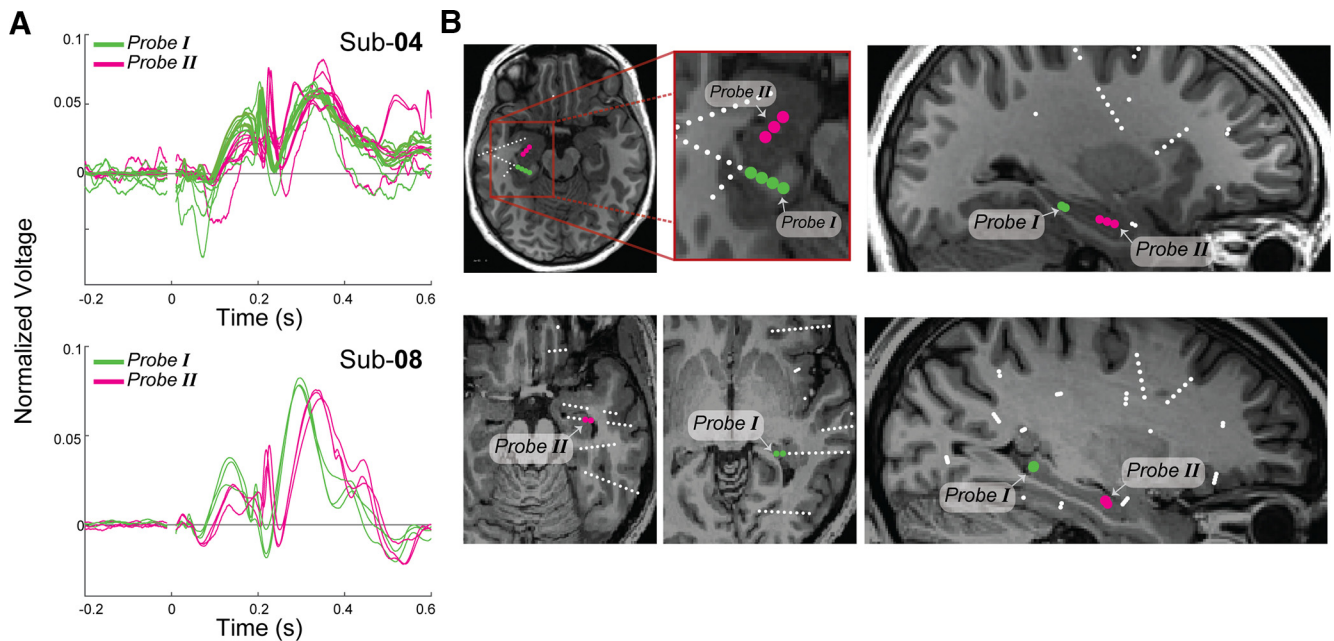


**Figure 6.** Location of HC stimulation sites and latency of PCC responses. **A**, Normalized limbic HAP-waves (L2 normalized) measured in PCC after HC stimulation are plotted as a function of time for subjects 4 (Sub-04) and 8 (Sub-08). Significant limbic HAP-waves on stimulation of Probe I (in green) and Probe II (in magenta). **B**, Axial (left) and sagittal (right) view with an estimation of the stimulated electrodes (contacts in Probe I in green; contacts in Probe II in magenta).

$\text{ph}_{\text{cin}}$  (orange tract), and  $\text{po}_{\text{cin}}$  (blue tract), as shown in previous anatomic studies (Jones et al., 2013; Wu et al., 2016; Bubb et al., 2018). The mammillary bodies-ANT connection through the mammillothalamic tract (Fig. 7, red dotted line) is not estimated in our study, as it would require longer and more advanced scanning techniques (Kamali et al., 2018) or additional anatomic sequences (Grewal et al., 2018; Grodd et al., 2020).

We analyze waveforms from subjects 2 and 7 with electrodes implanted in the ANT trying to differentiate the pathway potentially involved in the propagation of the limbic HAP-wave. All possible ANT-to-PCC connections are significant with a clear limbic HAP-wave morphology (Fig. 7B, green traces). To quantify the delay between the limbic HAP-waves measured in the PCC after ANT and HC stimulation, we calculate the cross-correlation between the average of the HC-to-PCC and ANT-to-PCC limbic HAP-waves (Fig. 7C). The ANT-to-PCC connections show a significantly earlier latency compared with the HC-to-PCC limbic HAP-waves (confidence intervals calculated by bootstrapping with 10,000 resamples), with an average shift of 37 ms in subject 2 and 102 ms in subject 7. The 37 ms delay observed in subject 2 is a typical delay between distant regions (Keller et al., 2014), and the 102 ms delay in subject 7 also has a larger confidence interval given that the HC stimulations at 4 mA are less robust. The decreased latency of the limbic HAP-wave after ANT stimulation suggests an anterior route of propagation, potentially traveling from HC, through the fornix to the ANT, and later through the parolfactory cingulum bundle to the PCC, (Wu et al., 2016; Wang et al., 2020).

By looking at the visual match among the electrode positions, estimated bundles, and their end points, in addition to the presence of the limbic HAP-wave after ANT stimulation, we hypothesize that the limbic HAP-wave is generated by the circuit among the HC, ANT, and the PCC, consistent with the previous reports on the hippocampal limbic system (Rolls, 2015; Wang et al., 2020; Aggleton et al., 2022). Interestingly, limbic HAP-waves in the PCC are not as clearly observed in subject 7 under HC

stimulation (Fig. 7A, orange traces), whereas ANT stimulation evoked clear limbic HAP-waves. We note that the stimulation amplitude in subject 7 was lower when stimulating the HC compared with ANT and compared with the one used for the other subjects (4 mA compared with 6 mA). Thus, a lower amplitude results in a smaller volume of tissue activation, perhaps not stimulating the hippocampus or fornix as strongly as in other cases.

### Limbic connections

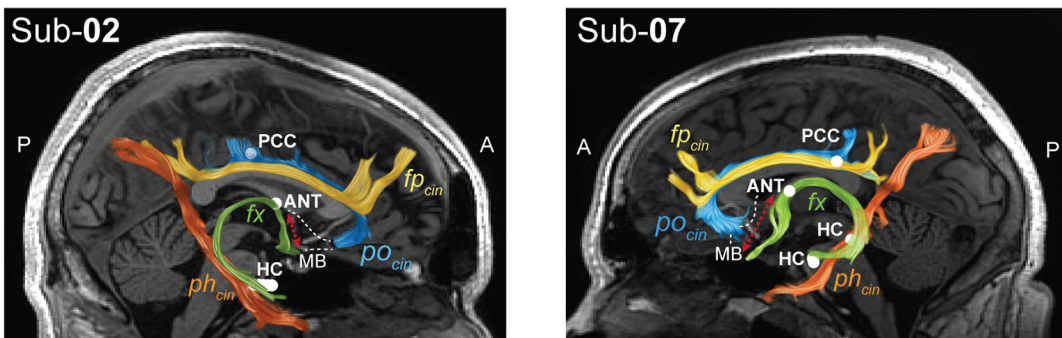
We report the limbic HAP-wave, an electrophysiological signature in the PCC when stimulating in the HC or ANT. This limbic HAP-wave is visually distinct from other waveforms, including those with strong effective and functional connectivity, such as the amygdala-to-ACC (Beckmann et al., 2009; Rolls, 2015; Bubb et al., 2018; Oane et al., 2020). To quantify the distinction between these two functional networks (memory and spatial HC-to-PCC and the emotional amygdala-to-ACC connections), we performed an LDA on principal components of discrete wavelet-transformed CCEPs (see Materials and Methods; Fig. 8). The second and third principal components, which collectively explained 42% of total variance across waveforms, are used for LDA as they independently show highest separation between HC-to-PCC and amygdala-to-ACC conditions (training accuracy, 78.0%; Fig. 8B, right). Figure 8C shows that HC-to-PCC waveforms (blue) cluster distinctly from amygdala-to-ACC (red) waveforms. The leave-one-subject-out cross-validation accuracy of LDA between these two conditions is 79.7%, on average. This was significantly greater than expected by chance, as determined by permutation testing (Fig. 8D). Four of the eight left-out subjects show individual test accuracies that were significantly greater than expected by chance as well, subject to a 5% false discovery rate. The other limbic conditions are more interspersed in the two-dimensional representation.

Cross-validation accuracy of the above model is superior to LDAs performed on principal components of unfiltered and filtered time domain waveforms (Extended Data Fig. 8-1). In each

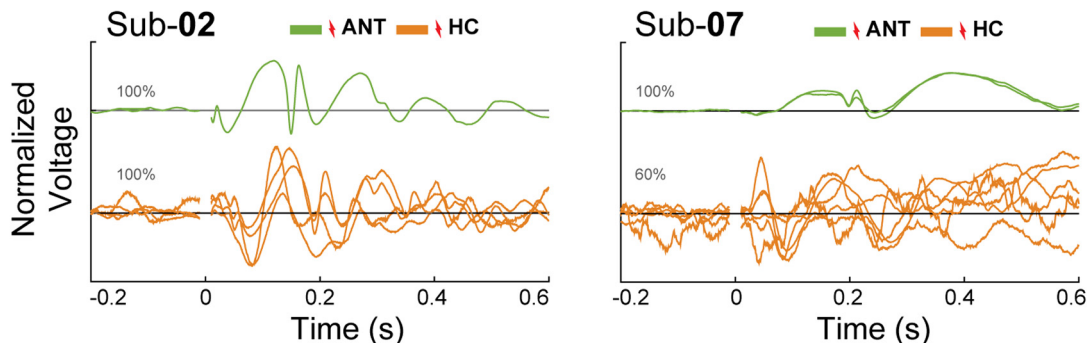
## Network propagation of the limbic-H-wave

**A**

### dMRI HC-PCC tractography

**B**

### CCEPs in the PCC from ANT or HC stimulation

**C**

### Cross correlation and time shift

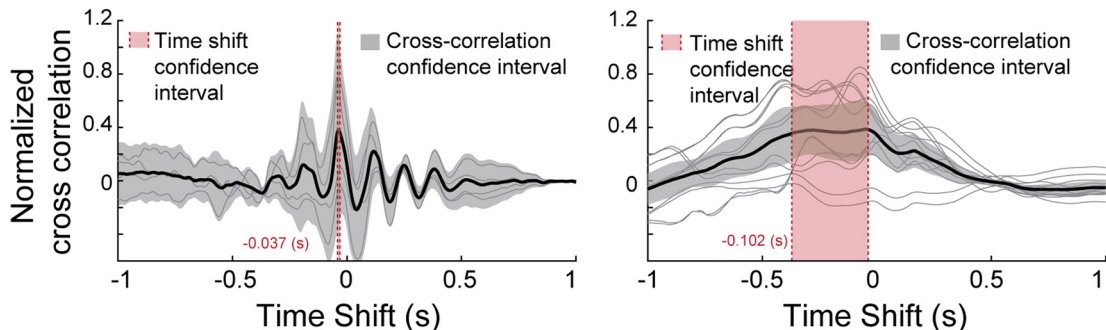


**Figure 7.** Limbic H-waves under ANT stimulation with reduced latencies suggests an anterior propagation route. **A**, dMRI estimates of the fx (green tract), ph<sub>cin</sub> (orange tract), fp<sub>cin</sub> (yellow), and po<sub>cin</sub> (blue), and estimated locations of the recording and stimulation sites in the PCC, HC, and ANT (white circles). Additionally, the representative mammillothalamic tract (dotted red line) connecting the MB and the ANT is shown. **B**, L2-normalized PCC CCEPs under ANT (green) and hippocampal (orange) stimulation, plotted over time. **C**, Normalized cross-correlations over time shift in seconds. Single cross-correlations (gray) and their average (black, 95% confidence interval, transparent gray). CCEPs in the PCC time shift after ANT stimulation compared with HC stimulation (95% confidence interval, transparent red). Sub-02, Subject 2; Sub-07, subject 7.

case, the LDA is performed on the two principal components that independently show the highest separation between the HC-to-PCC and amygdala-to-ACC conditions, as above. This corresponded to principal components 1 and 2 for the unfiltered, <8 and <13 Hz low pass-filtered, and  $\theta$  bandpass-filtered conditions; principal components 1 and 3 for the <4 Hz low pass-filtered condition; principal components 3 and 4 for the  $\alpha$  bandpass-filtered condition; and principal components 3 and 5 for the  $\beta$  bandpass-filtered condition. The mean cross-validation accuracy is ~60% for each of the unfiltered and low pass-filtered conditions, indicating that reduction of high-frequency noise alone does not improve the separability of HC-to-PCC and amygdala-to-ACC CCEPs. The  $\theta$  bandpass-filtered waveforms show the highest mean cross-validation accuracy of

72.0% of all filtering conditions, second only to the discrete wavelet transformed condition above. The relatively high accuracy obtained using the  $\theta$  band is likely attributable to the similarity between the length of the  $\theta$  band half-period (62.5–125 ms) and the durations of meaningful aperiodic peaks and troughs in the limbic waveforms, rather than to the presence of true oscillatory behavior. The alpha and beta bandpass-filtered conditions result in worse cross-validation accuracies of 64.7% and 57.1%, respectively.

## Discussion

To map network signatures in limbic subsystems, we measured single-pulse stimulation-evoked electrophysiological waveforms

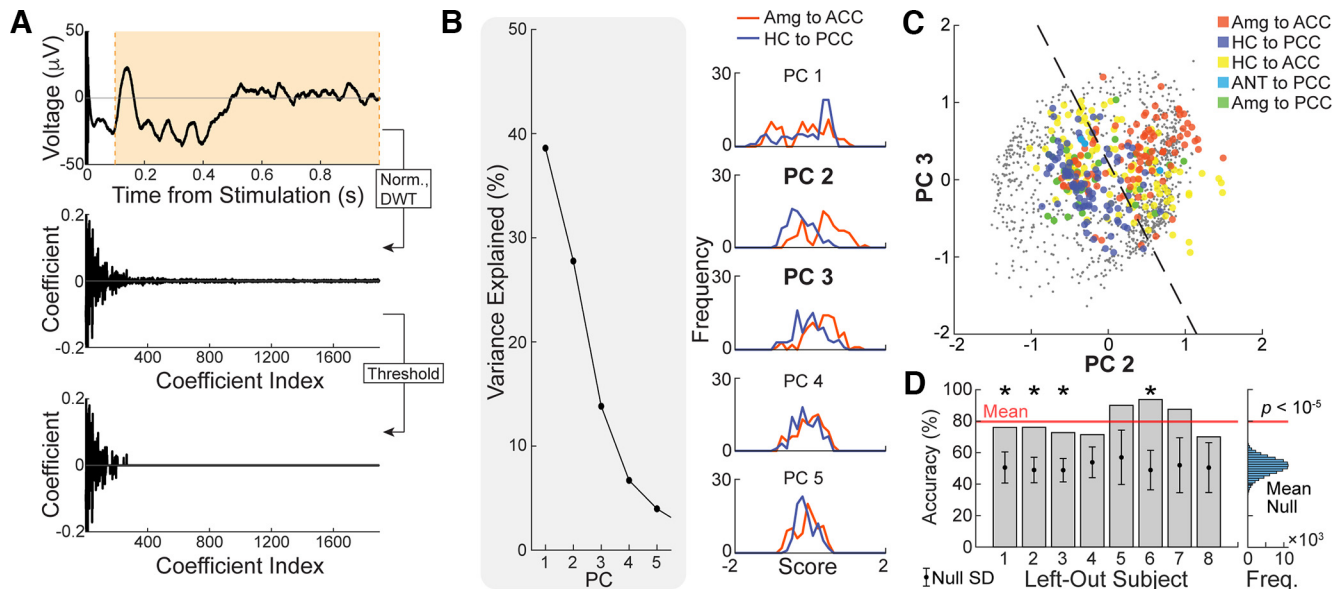


**Figure 8.** Similarity metrics within tested limbic connections. **A**, Each significant limbic CCEP was L2 normalized between 100 and 500 ms poststimulation and then subject to a level-8 (maximum) discrete wavelet transform using the fourth Symlet wavelet. All wavelet coefficients below the 95% percentile were set to 0. **B**, Principal component analysis was performed on all thresholded and discrete wavelet-transformed CCEPs. Left, Percentage of variance explained by each of the first five principal components. Right, Distribution of amygdala-to-ACC and hippocampus-to-PCC scores in each of the first five principal components. **C**, All limbic CCEPs were projected to the second and third principal components (PCs), which exhibited the greatest independent separation of amygdala-to-ACC and hippocampus-to-PCC CCEPs. Dashed line indicates the decision boundary for linear discriminant analysis between amygdala-to-ACC and hippocampus-to-PCC CCEPs. Training accuracy = 78.0%. **D**, Leave-one-subject-out cross-validation yielded a mean accuracy of 79.7% (red line). Left, Bars show the test accuracy for each left-out subject, while circle and error bars show the mean and SD of the null test accuracy distribution for the same left-out subject by permutation testing. An asterisk (\*) indicates significantly higher accuracy than expected by chance at an FDR of 0.05. Right, The histogram shows the mean cross-validation accuracy, across all subjects, for each permutation of the null model. Cross-validation accuracies for the models trained and tested on filtered temporal data are shown in Extended Data Figure 8-1, for comparison. Freq., Frequency; Norm., Normalized; DWT, Discrete Wavelet Transform.

from the human limbic system across the full duration of the response (1 s), well beyond previously characterized early responses (<100 ms). Our data show different stimulation-driven waveforms when stimulating and recording from different limbic regions. We describe how the limbic HAP-wave, measured in PCC after HC or ANT stimulation, as follows: (1) shows reliable timing and morphology across trials with a peak at ~200 ms; (2) shares similar, decodable features across subjects; (3) has reversed polarity across superficial and deep cortical PCC recording sites; and (4) has a decrease in latency of the response at a recorded end point when stimulating further downstream in the HC or in the ANT. Following these criteria, we characterize a distinctive limbic HAP-wave present in indirect HC-ANT-PCC connections that is likely related to the memory and spatial hippocampal subsystem of the limbic network.

#### Responses in the memory and spatial limbic subsystem

Using the limbic system as a canonical circuit for investigation demonstrates that CCEPs can map out network signatures in cognitive brain circuits, such as the hippocampal limbic subsystem associated with memory and spatial processing. Our findings indicate that the CCEPs in the PCC after HC stimulation have a distinct waveform with a sharp peak at ~200 ms preceded and followed by slow waves. These late responses are likely generated through polysynaptic indirect cortico-subcortical connections (Child and Benarroch, 2013; Kubota et al., 2013; Kumaravelu et al., 2018). Brain structures involved in the propagation of the limbic HAP-wave, such as hippocampus, ANT, and PCC, have been described as part of the Papez (1937) circuit, and were later associated with a distinct functional role in memory and spatial processing within the limbic system (Rolls, 2015; Bubb et al., 2017).

The dMRI data indicate the white matter tracts that potentially mediate the propagation of the limbic HAP-wave. The stimulated and recorded electrode sites matched the fornix and parolfactory cingulum bundle end points, respectively. Diffusion MRI studies have started to delineate different parts of the cingulum bundle in humans (Beckmann et al., 2009; Jones et al., 2013; Wu et al., 2016). The parolfactory cingulum bundle connects subgenual regions to the PCC, consistent with what has been shown in animal studies (Mufson and Pandya, 1984; Carmichael and Price, 1996; Wu et al., 2016; Bubb et al., 2018). Given the end point location of our electrodes, the  $p_{ocin}$  segment of the cingulum is most likely involved in the limbic HAP-wave, in contrast with the  $fp_{cin}$  and  $ph_{cin}$  segments of the cingulum, where the end points are located more posterior from the electrodes. Future animal, lesion, and stimulation studies may further explain the network involved in the limbic HAP-wave and how its later components are being generated.

It is important to distinguish the connections from amygdala and ACC versus from HC and PCC to understand limbic subsystems (Rolls, 2015). Recent functional studies further emphasize the subdivisions of the cingulate cortex and cytoarchitectural differences (Aponik-Gremillion et al., 2022; Willbrand et al., 2022). Our results show that inputs to PCC are more reliable from the hippocampus compared with amygdala and that this was not the case in ACC. Moreover, we trained a model that showed a distinction between HC-to-PCC connections (related to the hippocampal limbic system) and amygdala-to-ACC connections (related to the emotion limbic system) based on its waveform. This indicates that electrical stimulation-evoked waveforms are particular for different anatomic connections and may potentially serve as biomarkers of different anatomic and functional limbic subsystems, in a similar manner as other studies have done in the motor system.

The HAP-wave reported in this study could typically be observed at the single-trial level in each subject. While future studies may include more subjects or stimulations per electrode to extract other, smaller CCEPs that are only apparent on averaging across a larger number of trials, the amplitude and reliability of the limbic HAP-wave allowed us to look at the variability within subjects. Variability within subjects shows how unique electrophysiological responses vary in amplitude, polarity, and latency depending on the stimulated and measured electrode. The high temporal and spatial resolution of the sEEG recordings described here allow us to delineate how shifts in polarity and latency can be explained by the cortical layer of the recording electrode and the distance between the recording and stimulated site.

Previous CCEP studies have primarily described the early evoked responses by focusing on (1) changes in strength (root mean square) or on (2) the N1 or first positive component (Kubota et al., 2013; Enatsu et al., 2015; Donos et al., 2016; Takeyama et al., 2019; Oane et al., 2020). Kubota et al. (2013) and Enatsu et al. (2015) reported strong CCEPs in the PCC after both anterior and posterior HC stimulation. While their results thus focus on the early responses, a review of their figures reveals a similar waveform within the first 300 ms that is similar to the limbic HAP-wave in our data. Another study similarly showed a peak in the PCC at 187 ms after fornix stimulation (Koubeissi et al., 2013). While neither study elaborated on this waveform, they provide independent confirmation of our measurements. Thus, the limbic HAP-wave in our data is therefore reproducible across studies and emphasizes that different networks may show unique interactions.

### Stimulation driven signatures as biomarkers

In motor systems, Patton and Amassian (1954) described D-waves as early or direct responses, in contrast with the later or indirect I-waves. These well characterized waveforms are used as biomarkers for intraoperative monitoring to understand and diagnose pathology in the motor functions (Boyd et al., 1986; Hicks et al., 1991; Quinones-Hinojosa et al., 2005; Costa et al., 2013). In the limbic system, such waveforms thus far have not been characterized. The limbic HAP-wave we observed may characterize an indirect anterior route within the limbic network (Papez, 1937; Rolls, 2015) from hippocampus, through the fornix to the mammillary bodies, through the mammillothalamic tract to ANT, through the parolfactory segment of the cingulum bundle to the PCC (Fig. 7).

Epilepsy often involves the limbic system (Wyllie, 2012). In our study, only subjects 6 and 8 had a limbic SOZ (see Materials and Methods, subsection Subjects), and subjects 4 and 8 had reported interictal activity in the PCC (Table 1, interictal notes). However, all eight subjects had reported interictal epileptiform activity involving the hippocampus or amygdala, which is typical for patients who have electrodes implanted in the limbic system. Interictal epileptiform spike slow-wave discharges have been reported in the cerebral cortex in animals behaving freely (Pearce et al., 2014), and are typically considered a hallmark of hyperexcitability associated with epilepsy (Williams, 1953; Babb and Crandall, 1976; Valentín et al., 2002, 2005). The limbic HAP-wave morphology as presented in Figure 3 resembles to some extent an interictal spike-wave discharge, which is commonly seen in both scalp and invasive EEG monitoring. Spontaneous examples may occur as single examples or in trains. The observed limbic HAP-wave contains a single cycle, had reliable latency across trials and subjects,

shows specificity to the PCC, and was not seen between hippocampus and amygdala (Extended Data Figs. 2–3, 2–4), in distinction from more commonly reported stimulation-evoked afterdischarges. While epilepsy and a hyperexcitable limbic system may therefore facilitate this response, future research will have to determine to what extent it is only observed in patients with epilepsy.

### Conclusion

Single-pulse electrical stimulation reveals the limbic HAP-wave in the PCC after stimulating the HC. Combined with diffusion imaging, and well established anatomic knowledge (Papez, 1937; Wang et al., 2020), we suggest that this response may be generated by indirect projections through the hippocampal limbic system. Stimulation-generated waveforms have been used for many decades as electrophysiological biomarkers of motor system function. These data suggest that the limbic HAP-wave we describe can be used as such an electrophysiological biomarker of the memory–spatial part of the limbic system.

### References

- Aggleton JP, Nelson AJD, O'Mara SM (2022) Time to retire the serial Papez circuit: implications for space, memory, and attention. *Neurosci Biobehav Rev* 140:104813.
- Aponik-Gremillion L, Chen YY, Bartoli E, Koslov SR, Rey HG, Weiner KS, Yoshor D, Hayden BY, Sheth SA, Foster BL (2022) Distinct population and single-neuron selectivity for executive and episodic processing in human dorsal posterior cingulate. *Elife* 11:e80722.
- Awiszus F, Feistner H (1994) Quantification of D- and I-wave effects evoked by transcranial magnetic brain stimulation on the tibialis anterior motoneuron pool in man. *Exp Brain Res* 101:153–158.
- Babb TL, Crandall PH (1976) Epileptogenesis of human limbic neurons in psychomotor epileptics. *Electroencephalogr Clin Neurophysiol* 40:225–243.
- Beckmann M, Johansen-Berg H, Rushworth MF (2009) Connectivity-based parcellation of human cingulate cortex and its relation to functional specialization. *J Neurosci* 29:1175–1190.
- Benjamini Y, Yekutieli D (2001) The control of the false discovery rate in multiple testing under dependency. *Ann Stat* 29:1165–1188.
- Bertram EH, Zhang DX, Mangan P, Fountain N, Rempe D (1998) Functional anatomy of limbic epilepsy: a proposal for central synchronization of a diffusely hyperexcitable network. *Epilepsy Res* 32:194–205.
- Borchers S, Himmelbach M, Logothetis N, Karnath H-O (2011) Direct electrical stimulation of human cortex, gold standard for mapping brain functions. *Nat Rev Neurosci* 13:63–70.
- Boyd SG, Rothwell JC, Cowan JMA, Webb PJ, Morley T, Asselman P, Marsden CD (1986) A method of monitoring function in corticospinal pathways during scoliosis surgery with a note on motor conduction velocities. *J Neurol Neurosurg Psychiatry* 49:251–257.
- Brunton SL, Kutz JN (2022) Data-driven science and engineering: machine learning, dynamical systems, and control. Cambridge, UK: Cambridge UP.
- Bubb EJ, Kinnanane L, Aggleton JP (2017) Hippocampal - diencephalic - cingulate networks for memory and emotion: an anatomical guide. *Brain Neurosci Adv* 1:2398212817723443.
- Bubb EJ, Metzler-Baddeley C, Aggleton JP (2018) The cingulum bundle: anatomy, function, and dysfunction. *Neurosci Biobehav Rev* 92:104–127.
- Carmichael ST, Price JL (1996) Connectional networks within the orbital and medial prefrontal cortex of macaque monkeys. *J Comp Neurol* 371:179–207.
- Child ND, Benaroch EE (2013) Anterior nucleus of the thalamus: functional organization and clinical implications. *Neurology* 81:1869–1876.
- Cieslak M, et al. (2021) QSIprep: an integrative platform for preprocessing and reconstructing diffusion MRI data. *Nat Methods* 18:775–778.
- Cogan SF, Ludwig KA, Welle CG, Takemakov P (2016) Tissue damage thresholds during therapeutic electrical stimulation. *J Neural Eng* 13:021001.
- Costa P, Peretta P, Faccani G (2013) Relevance of intraoperative D wave in spine and spinal cord surgeries. *Eur Spine J* 22:840–848.
- Daubechies I (1992) Ten lectures on wavelets. Philadelphia: SIAM.

- Destrieux C, Fischl B, Dale A, Halgren E (2010) Automatic parcellation of human cortical gyri and sulci using standard anatomical nomenclature. *Neuroimage* 53:1–15.
- Donos C, Mălia MD, Mindruță I, Popa I, Ene M, Bălănescu B, Ciurea A, Barborica A (2016) A connectomics approach combining structural and effective connectivity assessed by intracranial electrical stimulation. *Neuroimage* 132:344–358.
- Efron B, Tibshirani R (1998) An introduction to the bootstrap. London/Boca Raton, FL: Chapman and Hall/CRC.
- Enatsu R, Gonzalez-Martinez J, Bulacio J, Kubota Y, Mosher J, Burgess RC, Najm I, Nair DR (2015) Connections of the limbic network: a cortico-cortical evoked potentials study. *Cortex* 62:20–33.
- Fischl B (2012) FreeSurfer. *Neuroimage* 62:774–781.
- Fischl B, Dale AM (2000) Measuring the thickness of the human cerebral cortex from magnetic resonance images. *Proc Natl Acad Sci USA* 97:11050–11055.
- Foo TKF, et al. (2018) Lightweight, compact, and high-performance 3T MR system for imaging the brain and extremities. *Magn Reson Med* 80:2232–2245.
- Friston KJ, Ashburner J, Kiebel S, Nichols T, Penny WD (2007) Statistical parametric mapping: the analysis of functional brain images, Ed 1. Amsterdam/Boston: Elsevier/Academic.
- Gregg NM, Sladky V, Nejedly P, Mivalt F, Kim I, Balzekas I, Sturges BK, Crowe C, Patterson EE, Van Gompel JJ, Lundstrom BN, Leyde K, Denison TJ, Brinkmann BH, Kremen V, Worrell GA (2021) Thalamic deep brain stimulation modulates cycles of seizure risk in epilepsy. *Sci Rep* 11:24250.
- Grewal SS, Middlebrooks EH, Kaufmann TJ, Stead M, Lundstrom BN, Worrell GA, Lin C, Baydin S, Van Gompel JJ (2018) Fast gray matter acquisition T1 inversion recovery MRI to delineate the mammillothalamic tract for preoperative direct targeting of the anterior nucleus of the thalamus for deep brain stimulation in epilepsy. *Neurosurg Focus* 45:E6.
- Grodd W, Kumar VJ, Schütz A, Lindig T, Scheffler K (2020) The anterior and medial thalamic nuclei and the human limbic system: tracing the structural connectivity using diffusion-weighted imaging. *Sci Rep* 10:10957.
- Gronlier E, Vendramini E, Volle J, Wozniak-Kwasniewska A, Antón Santos N, Coizet V, Duveau V, David O (2021) Single-pulse electrical stimulation methodology in freely moving rat. *J Neurosci Methods* 353:109092.
- Gupta MR, Jacobson NP (2006) Wavelet principal component analysis and its application to hyperspectral images. In: Proceedings of 2006 international conference on image processing, pp 1585–1588. New York, NY: IEEE.
- Hermes D, Miller KJ, Noordmans HJ, Vansteensel MJ, Ramsey NF (2010) Automated electrocorticographic electrode localization on individually rendered brain surfaces. *J Neurosci Methods* 185:293–298.
- Hicks RG, Burke DJ, Stephen JPH (1991) Monitoring spinal-cord function during scoliosis surgery with cotrel-dubousset instrumentation. *Med J Aust* 154:82–86.
- Holtzheimer PE, Kelley ME, Gross RE, Filkowski MM, Garlow SJ, Barrocas A, Wint D, Craighead MC, Kozarsky J, Chismar R, Moreines JL, Mewes K, Posse PR, Gutman DA, Mayberg HS (2012) Subcallosal cingulate deep brain stimulation for treatment-resistant unipolar and bipolar depression. *Arch Gen Psychiatry* 69:150–158.
- Huang H, Gregg NM, Valencia GO, Brinkmann BH, Lundstrom BN, Worrell GA, Miller KJ, Hermes D (2023) Electrical stimulation of temporal and limbic circuitry produces distinct responses in human ventral temporal cortex. *J Neurosci* 43:4434–4447.
- In M-H, Tan ET, Trzasko JD, Shu Y, Kang D, Yarach U, Tao S, Gray EM, Huston J 3rd, Bernstein MA (2020) Distortion-free imaging: a double encoding method (DIADEM) combined with multiband imaging for rapid distortion-free high-resolution diffusion imaging on a compact 3T with high-performance gradients. *J Magn Reson Imaging* 51:296–310.
- Innocenti GM, Vercelli A, Caminiti R (2014) The diameter of cortical axons depends both on the area of origin and target. *Cereb Cortex* 24:2178–2188.
- Jo HJ, Kenney-Jung DL, Balzekas I, Welker KM, Jones DT, Croarkin PE, Benarroch EE, Worrell GA (2019) Relationship between seizure frequency and functional abnormalities in limbic network of medial temporal lobe epilepsy. *Front Neurol* 10:488.
- Jones DK, Christiansen KF, Chapman RJ, Aggleton JP (2013) Distinct subdivisions of the cingulum bundle revealed by diffusion MRI fibre tracking: implications for neuropsychological investigations. *Neuropsychologia* 51:67–78.
- Kahn L, Sutton B, Winston HR, Abosch A, Thompson JA, Davis RA (2021) Deep brain stimulation for obsessive-compulsive disorder: real world experience post-FDA-humanitarian use device approval. *Front Psychiatry* 12:56932.
- Kamali A, Zhang CC, Riascos RF, Tandon N, Bonafante-Mejia EE, Patel R, Lincoln JA, Rabiei P, Ocasio L, Younes K, Hasan KM (2018) Diffusion tensor tractography of the mammillothalamic tract in the human brain using a high spatial resolution DTI technique. *Sci Rep* 8:5229.
- Keller CJ, Honey CJ, Mégevand P, Entz L, Ulbert I, Mehta AD (2014) Mapping human brain networks with cortico-cortical evoked potentials. *Philos Trans R Soc Lond B Biol Sci* 369:20130528.
- Koubeissi MZ, Kahriman E, Syed TU, Miller J, Durand DM (2013) Low-frequency electrical stimulation of a fiber tract in temporal lobe epilepsy. *Ann Neurol* 74:223–231.
- Kubota Y, Enatsu R, Gonzalez-Martinez J, Bulacio J, Mosher J, Burgess RC, Nair DR (2013) In vivo human hippocampal cingulate connectivity: a cortico-cortical evoked potentials (CCEPs) study. *Clin Neurophysiol* 124:1547–1556.
- Kumaravelu K, Oza CS, Behrend CE, Grill WM (2018) Model-based deconstruction of cortical evoked potentials generated by subthalamic nucleus deep brain stimulation. *J Neurophysiol* 120:662–680.
- Lockman J, Fisher RS (2009) Therapeutic brain stimulation for epilepsy. *Neurol Clin* 27:1031–1040.
- Lozano AM, Lipsman N, Bergman H, Brown P, Chabardes S, Chang JW, Matthews K, McIntyre CC, Schlaepfer TE, Schulder M, Temel Y, Volkman J, Krauss JK (2019) Deep brain stimulation: current challenges and future directions. *Nat Rev Neurol* 15:148–160.
- Luke SG (2017) Evaluating significance in linear mixed-effects models in R. *Behav Res Methods* 49:1494–1502.
- Luo Y, Sun Y, Tian X, Zheng X, Wang X, Li W, Wu X, Shu B, Hou W (2021) Deep brain stimulation for Alzheimer's disease: stimulation parameters and potential mechanisms of action. *Front Aging Neurosci* 13:619543.
- MacLean PD (1949) Psychosomatic Disease and the "Visceral Brain": Recent Developments Bearing on the Papez Theory of Emotion. *Psychosomatic medicine* 11:338–353.
- Matsumoto R, Nair DR, LaPresto E, Najm I, Bingaman W, Shibasaki H, Lüders HO (2004) Functional connectivity in the human language system: a cortico-cortical evoked potential study. *Brain* 127:2316–2330.
- Mercier MR, et al. (2022) Advances in human intracranial electroencephalography research, guidelines and good practices. *Neuroimage* 260:119438.
- Miller KJ, Prieto T, Williams NR, Halpern CH (2019) Case Studies in Neuroscience: the electrophysiology of a human obsession in nucleus accumbens. *J Neurophysiol* 121:2336–2340.
- Miller KJ, Müller KR, Valencia GO, Huang H, Gregg NM, Worrell GA, Hermes D (2023) Canonical response parameterization: quantifying the structure of responses to single-pulse intracranial electrical brain stimulation. *PLoS Comput Biol* 19:e1011105.
- Mitzdorf U (1985) Current source-density method and application in cat cerebral-cortex - investigation of evoked-potentials and EEG phenomena. *Physiol Rev* 65:37–100.
- Mufson EJ, Pandya DN (1984) Some observations on the course and composition of the cingulum bundle in the rhesus-monkey. *J Comp Neurol* 225:31–43.
- Nair DR, et al. (2020) Nine-year prospective efficacy and safety of brain-responsive neurostimulation for focal epilepsy. *Neurology* 95:e1244–e1256.
- Nemanic S, Alvarado MC, Bachevalier J (2004) The hippocampal/parahippocampal regions and recognition memory: insights from visual paired comparison versus object-delayed nonmatching in monkeys. *J Neurosci* 24:2013–2026.
- Oane I, Barborica A, Chetan F, Donos C, Mălia MD, Arbune AA, Daneasa A, Pistol C, Nica AE, Bajenaru OA, Mindruță I (2020) Cingulate cortex function and multi-modal connectivity mapped using intracranial stimulation. *Neuroimage* 220:117059.
- Pal Attia T, Crepeau D, Kremen V, Nasseri M, Guragain H, Steele SW, Sladky V, Nejedly P, Mivalt F, Herron JA, Stead M, Denison T, Worrell GA, Brinkmann BH (2021) Epilepsy personal assistant device—a mobile platform for brain state, dense behavioral and physiology tracking and controlling adaptive stimulation. *Front Neurol* 12:704170.
- Papez JW (1937) A proposed mechanism of emotion. *Arch Neuropsych* 38:725–774.

- Patton HD, Amassian VE (1954) Single and multiple-unit analysis of cortical stage of pyramidal tract activation. *J Neurophysiol* 17:345–363.
- Pearce PS, Friedman D, Lafrancos JJ, Iyengar SS, Fenton AA, Maclusky NJ, Scharfman HE (2014) Spike-wave discharges in adult Sprague-Dawley rats and their implications for animal models of temporal lobe epilepsy. *Epilepsy Behav* 32:121–131.
- Prime D, Rowlands D, O'Keefe S, Dionisio S (2018) Considerations in performing and analyzing the responses of cortico-cortical evoked potentials in stereo-EEG. *Epilepsia* 59:16–26.
- Prime D, Woolfe M, O'Keefe S, Rowlands D, Dionisio S (2020) Quantifying volume conducted potential using stimulation artefact in cortico-cortical evoked potentials. *J Neurosci Methods* 337:108639.
- Puyati W, Walairacht S, Walairacht A (2006) PCA in wavelet domain for face recognition. In: Proceedings of the 2006 8th international conference advanced communication technology: toward the era of ubiquitous networks and societies. Phoenix Park, South Korea: National Computerization Agency.
- Quinones-Hinojosa A, Lyon R, Zada G, Lamborn KR, Gupta N, Parsa AT, McDermott MW, Weinstein PR (2005) Changes in transcranial motor evoked potentials during intramedullary spinal cord tumor resection correlate with postoperative motor function. *Neurosurgery* 56:982–993.
- Rolls ET (2015) Limbic systems for emotion and for memory, but no single limbic system. *Cortex* 62:119–157.
- Salanova V, et al. (2015) Long-term efficacy and safety of thalamic stimulation for drug-resistant partial epilepsy. *Neurology* 84:1017–1025.
- Siddiqi SH, et al. (2021) Brain stimulation and brain lesions converge on common causal circuits in neuropsychiatric disease. *Nat Hum Behav* 5:1707–1716.
- Squire LR (1998) History of neuroscience in autobiography. San Diego: Academic.
- Strange BA, Witter MP, Lein ES, Moser EI (2014) Functional organization of the hippocampal longitudinal axis. *Nat Rev Neurosci* 15:655–669.
- Takeyama H, Matsumoto R, Usami K, Nakae T, Kobayashi K, Shimotake A, Kikuchi T, Yoshida K, Kunieda T, Miyamoto S, Takahashi R, Ikeda A (2019) Human entorhinal cortex electrical stimulation evoked short-latency potentials in the broad neocortical regions: evidence from cortico-cortical evoked potential recordings. *Brain Behav* 9:e01366.
- Trebaul L, Rudrauf D, Job AS, Mălia MD, Popa I, Barborica A, Minotti L, Mindruță I, Kahane P, David O (2016) Stimulation artifact correction method for estimation of early cortico-cortical evoked potentials. *J Neurosci Methods* 264:94–102.
- Uher D, Klimes P, Cimbalnik J, Roman R, Pail M, Brazdil M, Jurak P (2020) Stereo-electroencephalography (SEEG) reference based on low-variance signals. *Annu Int Conf IEEE Eng Med Biol Soc* 2020:204–207.
- Valentín A, Anderson M, Alarcón G, Seoane JJ, Selway R, Binnie CD, Polkey CE (2002) Responses to single pulse electrical stimulation identify epileptogenesis in the human brain in vivo. *Brain* 125:1709–1718.
- Valentín A, Alarcón G, Honavar M, Garcia Seoane JJ, Selway RP, Polkey CE, Binnie CD (2005) Single pulse electrical stimulation for identification of structural abnormalities and prediction of seizure outcome after epilepsy surgery: a prospective study. *Lancet Neurol* 4:718–726.
- van Blooij D, van den Boom MA, van der Aar JF, Huiskamp GM, Castegnaro G, Demuru M, Zweiphenning W, van Eijnsden P, Miller KJ, Leijten FSS, Hermes D (2023) Developmental trajectory of transmission speed in the human brain. *Nat Neurosci* 26:537–541.
- Vogt BA (2019) Cingulate cortex in the three limbic subsystems. *Handb Clin Neurol* 166:39–51.
- Wang YC, Kremen V, Brinkmann BH, Middlebrooks EH, Lundstrom BN, Grewal SS, Guragain H, Wu MH, Van Gompel JJ, Klassen BT, Stead M, Worrell GA (2020) Probing circuit of Papez with stimulation of anterior nucleus of the thalamus and hippocampal evoked potentials. *Epilepsy Res* 159:106248.
- Willbrand EH, Parker BJ, Voorhies WI, Miller JA, Lyu I, Hallock T, Aponik-Gremillion L, Koslov SR, Bunge SA, Foster BL, Weiner KS (2022) Uncovering a tripartite landmark in posterior cingulate cortex. *Sci Adv* 8:eabn9516.
- Williams D (1953) A study of thalamic and cortical rhythms in petit mal. *Brain* 76:50–69.
- Wu H, Miller KJ, Blumenfeld Z, Williams NR, Ravikumar VK, Lee KE, Kakusa B, Sacchet MD, Wintermark M, Christoffel DJ, Rutt BK, Bronte-Stewart H, Knutson B, Malenka RC, Halpern CH (2018) Closing the loop on impulsivity via nucleus accumbens delta-band activity in mice and man. *Proc Natl Acad Sci U S A* 115:192–197.
- Wu Y, Sun D, Wang Y, Wang Y, Ou S (2016) Segmentation of the cingulum bundle in the human brain: a new perspective based on dsi tractography and fiber dissection study. *Front Neuroanat* 10:84.
- Wyllie E (2012) Wyllie's treatment of epilepsy: principles and practice, Ed 5. Philadelphia: Lippincott Williams & Wilkins.
- Yeh FC (2020) Shape analysis of the human association pathways. *Neuroimage* 223:117329.
- Yeh FC, Wedeen VJ, Tseng WY (2010) Generalized q-sampling imaging. *IEEE Trans Med Imaging* 29:1626–1635.
- Yeh FC, Verstynen TD, Wang Y, Fernández-Miranda JC, Tseng WY (2013) Deterministic diffusion fiber tracking improved by quantitative anisotropy. *PLoS One* 8:e80713.
- Yeh FC, Liu L, Hitchens TK, Wu YL (2017) Mapping immune cell infiltration using restricted diffusion MRI. *Magn Reson Med* 77:603–612.
- Yeh FC, Panesar S, Fernandes D, Meola A, Yoshino M, Fernandez-Miranda JC, Vettel JM, Verstynen T (2018) Population-averaged atlas of the macroscale human structural connectome and its network topology. *Neuroimage* 178:57–68.
- Yeh FC, Panesar S, Barrios J, Fernandes D, Abhinav K, Meola A, Fernandez-Miranda JC (2019) Automatic removal of false connections in diffusion MRI tractography using topology-informed pruning (TIP). *Neurotherapeutics* 16:52–58.